Nonpremixed Turbulent Reacting Flow near Extinction

Y. Y. LEE* **and S. B. POPE†**

Sibley School of Mechanical and Aerospace Engineering, Cornell University, Ithaca, NY 14853

Direct numerical simulations (DNS) are used to study fundamental processes in non-premixed turbulent reacting flows. A broad range of Damkohler number, Da, and reaction zone thicknesses are studied, encompassing: stable, near-equilibrium reaction; local extinction; and global extinction. A simple thermochemical model for one-step *reversible* reaction is employed, in which the state of the fluid is described by the mixture fraction $\xi(\mathbf{x}, t)$ and the perturbation from equilibrium $y(\mathbf{x}, t)$. A pseudo-spectral method, with grid sizes up to 128^3, is used to solve the Navier-Stokes equations and the conservation equations for ξ and y. These equations are augmented with artificial forcing, so that the resulting velocity and mixture fraction fields are statistically stationary, homogeneous and isotropic. At sufficiently high Damkohler number, the perturbation field is also statistically stationary, corresponding to stable reaction. But at lower Da, y increases without bound, corresponding to global extinction. The critical Damkohler number $\mathrm{Da}_{\mathrm{crit}}$ at which global extinction occurs is determined from the simulations, and is found to be significantly different from that predicted by simple models (flamelet, conditional moment closure, etc.). A simple statistical model is used to show that the discrepancy can plausibly be explained by statistical variability. The simulation results are used to assess the accuracy of simple models, especially for Damkohler numbers at which there is globally stable reaction, but significant local extinction.

1. INTRODUCTION

When the Damkohler number is very large, the fluid in a nonpremixed turbulent flame is everywhere close to chemical equilibrium: and theories and models based on the equilibrium assumption are successful [1, 2]. There are also a number of models that predict the small departures from equilibrium. Among these are: the flamelet model [3], two-variable assumed-pdf methods [4], pdf transport methods [5], quasi-equilibrium distributed reactions (QEDR) [6], and the conditional moment closure (CMC) [7, 8].

As the Damkohler number is decreased, the departures from equilibrium become larger, and local and global extinction can occur. These phenomena have been studied in a series of experiments on piloted jet diffusion flames by Masri et al. [9]. In these more testing circumstances, most of the models mentioned above either break down, or at least become much less secure. Calculations of the piloted jet flames—including local and global extinction—have been performed using pdf transport equations by Chen and Kollmann [10], Taing et al. [11], and Norris and Pope [12]. In spite of the partial success of these calculations, much remains to be learned about the detail processes involved in nonpremixed combustion far from equilibrium.

The objective of the present work is to use direct numerical simulations (DNS) to study nonpremixed turbulent reacting flows near extinction. Both the flow—constant-density, statistically stationary, homogeneous isotropic turbulence—and the thermochemistry—a one-step reversible reaction—are extremely simple, and yet they contain the required fundamental ingredients to display the competition between reaction and mixing which is the essence of the problem at hand.

In the simulations performed, the two parameters that are varied are the Damkohler number

$$\mathrm{Da} \equiv T_\chi / \tau^*, \tag{1}$$

(where T_χ and τ^* are the characteristic turbulent-mixing and reaction time scales, respectively) and the flame-thickness parameter

$$\xi^* \equiv \xi' / \Delta\xi_r, \tag{2}$$

(where ξ' is the rms mixture fraction and $\Delta\xi_r$ is the width of the reaction zone in mixture fraction space). At large Da, small values of ξ^*

* Present address: Mechanical Engineering, University of California, Irvine, CA 92717.

† Corresponding author.

COMBUSTION AND FLAME 101: 501–528 (1995)

Published by Elsevier Science Inc.

0010-2180/95/$9.50
SSDI 0010-2180(94)00240-S

(e.g., $\xi^* = 0.1$) correspond to broad reaction zones, whereas larger values (e.g. $\xi^* = 10$) correspond to thin flamelets.

Figure 1 is a sketch of the Da–ξ^* parameter plane. The equations governing the reacting flow (detailed in Section 3) are such that at sufficiently large Da a statistically stationary state exists corresponding to stable combustion. In this state, there is (on average) a balance between reaction and mixing. As the Damkohler number is decreased (by increasing the reaction time scale τ^*), the departure from equilibrium increases so as to maintain the average reaction rate. But, for given ξ^*, below a critical value of Da—$\mathrm{Da}_{\mathrm{crit}}(\xi^*)$—reaction can no longer balance mixing: in the simulations global extinction occurs, and at large times the reaction rate is zero.

The contributions of this work are: to identify the stability boundary $\mathrm{Da}_{\mathrm{crit}}(\xi^*)$; to present one-point statistics from simulations in the vicinity of this boundary; and to assess the accuracy of theories and models (namely, flamelet, QEDR and CMC) near this boundary.

The simulations (described in detail in Section 4) are performed using a pseudo-spectral method on grids of size up to 128^3. For inert flows, Taylor-scale Reynolds numbers R_λ in excess of 90 can be attained on 128^3 grids [13] with good resolution of the smallest (i.e., Kolmogorov) length scales. But thin reaction zones (large ξ^*) require resolution on scales smaller than the Kolmogorov scale, and hence (for a given grid) requires the Reynolds number to be reduced in order to maintain resolution. All the simulations reported here are at the rather low Reynolds number of $R_\lambda \approx 17$ so that fairly thin reaction zones can be simulated (i.e., ξ^* up to 1.5).

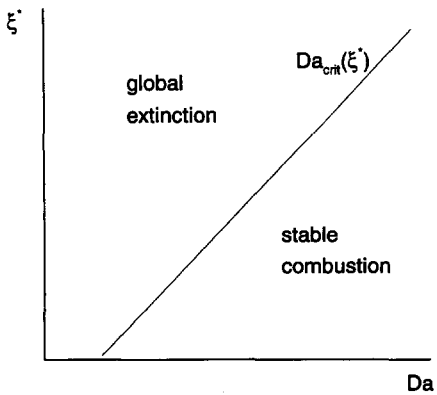

Fig. 1. Sketch of the Da – ξ^* parameter plane showing the line $\mathrm{Da}_{\mathrm{crit}}(\xi^*)$ that separates the region of stable combustion from that of global extinction.

The next three sections describe, in turn, the thermochemistry used, the governing equations, and the numerical simulation. In Section 5, the simulation results determining global extinction are presented. Several different models are outlined in Section 6, and their predictions of $\mathrm{Da}_{\mathrm{crit}}(\xi^*)$ are compared to the simulation data. The qualitative changes that occur in one-point statistics as Da is decreased from $\mathrm{Da} \gg \mathrm{Da}_{\mathrm{crit}}$ to $\mathrm{Da} \ll \mathrm{Da}_{\mathrm{crit}}$ are shown in Section 7. Then, in Section 8, the range of validity of different models is determined by quantifying the errors in their predictions as functions of Da and ξ^*.

2. THERMOCHEMISTRY

We consider the simplest possible thermochemistry that allows the study of finite-rate kinetic effects in non-premixed combustion. Accordingly, the density is taken to be constant ($\rho = 1$), and the molecular diffusivities Γ are taken to be equal and constant. The mixing is then completely characterized by the mixture fraction ξ. A one-step reversible reaction (fuel + oxidant $\rightleftharpoons$ product) is considered, with Y being the reaction progress variable (i.e. normalized mass fraction of product).

At equilibrium, Y adopts the value $Y_e(\xi)$ which is determined by the specified stoichiometric mixture fraction ξ_s ($0 < \xi_s < 1$) and by the specified equilibrium constant K ($K > [\xi_s(1-\xi_s)]^{-1}$). The equilibrium value $Y_e(\xi)$ is determined from the relation

$$K = \frac{Y_e^2}{\{\xi - \xi_s Y_e\}\{1 - \xi - (1-\xi_s)Y_e\}}. \qquad (3)$$

In the numerator, Y_e represents the mass fraction of products, while in the denominator the two terms in braces represent the mass fractions of fuel and oxidant, respectively.

It can be deduced from Eq. 3 that the maximum value of $Y_e(\xi), Y_{\max}$ is

$$Y_{\max} = \frac{1}{1 + 2/\sqrt{K}}, \tag{4}$$

which occurs at $\xi = \xi_{\max}$:

$$\xi_{\max} = \frac{\xi_s + K^{-1/2}}{1 + 2K^{-1/2}}. \tag{5}$$

As K tends to infinity it may be observed that $Y_{\max}$ tends to unity and $\xi_{\max}$ tends to ξ_s.

Different fuels can be simulated by different choices of ξ_s and K. For a real flame both ξ and Y lie between zero and unity. However, for purposes of DNS it is desirable to define the thermochemistry for all vales of ξ, and for negative values of Y. The specification given above leads to well-defined and sensible values of $Y_e(\xi)$ for all values of ξ.

In the theory of turbulent diffusion flames (e.g., Bilger [2]), the quantity

$$Y_e''(\xi) \equiv \frac{d^2 Y_e(\xi)}{d\xi^2}, \tag{6}$$

plays an important role. Figure 2 shows plots of $Y_e(\xi)$ and $Y_e''(\xi)$ for $\xi_s = 0.5$ and $K = 400$ —the values used in the simulations.

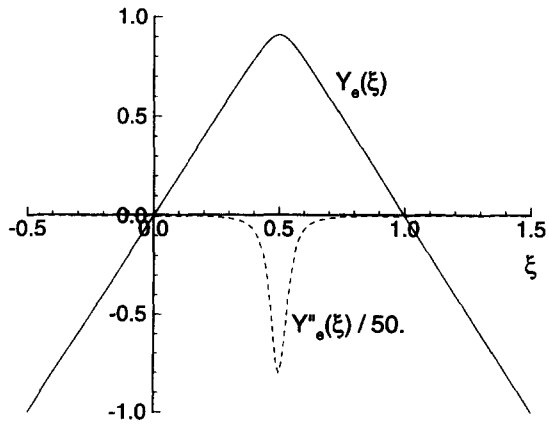

Fig. 2. Equilibrium value of Y, $Y_e(\xi)$, and its second derivative $Y_e''(\xi)$ against mixture fraction for $\xi_s = 0.5$, $K = 400$.

A central quantity in the present formulation is y—the departure from equilibrium of the reaction progress variable:

$$y = Y_e(\xi) - Y. \tag{7}$$

Without implication that it is small, y is referred to as the *perturbation*. The pair of variable (ξ, y) contains the same information as (ξ, Y). The perturbation y is zero for equilibrium, and otherwise positive.

The reaction rate S is defined as the rate of creation of Y. It is specified by

$$S_Y(\xi, Y) = S(\xi, y) = f(y)g(\xi)/\tau_c, \tag{8}$$

where τ_c is a specified time scale,

$$f(y) = By \exp(1 - By), \tag{9}$$

$$g(\xi) = \exp\{-B(Y_{\max} - Y_e(\xi))\}, \tag{10}$$

and B is a specified parameter—related to the activation energy—which here is ascribed the value $B = 15$. Both f and g are positive, with maximum values of unity. Figure 3 shows $f(y)$ for $B = 15$ while Fig. 4 shows $g(\xi)$ for $K = 400$. The makeup of the reaction rate is summarized for the chosen set of parameters on Fig. 5. The maximum reaction rate, which occurs at $(\xi, y) = (\xi_{\max}, B^{-1})$ is $S_{\max} = 1/\tau_c$. Although it is not based on a particular kinetic mechanism, this specification of $S(\xi, y)$ is designed to contain (in a mathematically simple way) the key ingredients of combustion chem-

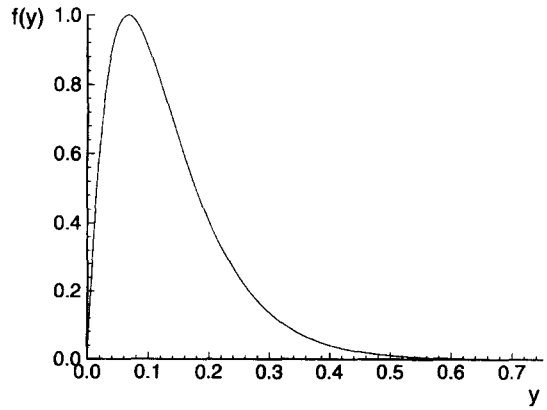

Fig. 3. Reaction rate function $f(y)$ (Eq. 9) versus the perturbation y, for $B = 15$.

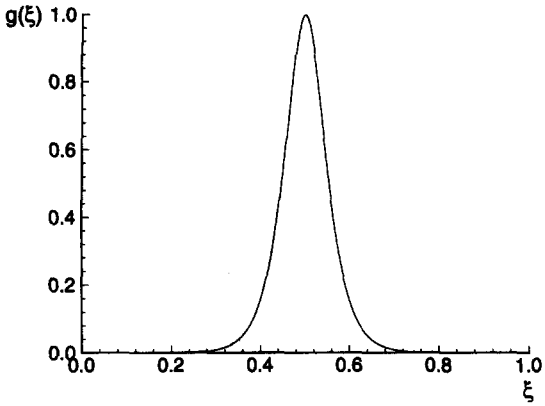

Fig. 4. Reaction rate function $g(\xi)$ (Eq. 10) versus mixture fraction for $\xi_s = 0.5$, $K = 400$, $B = 15$.

istry. These include: a linear dependence of S on y for small y; an exponential decrease for large y; and, a strong attenuation of S for mixtures far from stoichiometric.

Several derived quantities play important roles. The lean and rich limits of the reaction zone in mixture-fraction space (ξ_l and ξ_r) are defined to be the lower and upper values of ξ at which $g(\xi)$ equals 0.1. Then, the reaction zone thickness in mixture-fraction space is defined to be

$$\Delta\xi_r = \xi_r - \xi_l. \tag{11}$$

The quantity $S_0(\xi)$ is defined by

$$S_0(\xi) \equiv \left[\frac{\partial S(\xi, y)}{\partial y}\right]_{y=0} = g(\xi)/\tau^*, \tag{12}$$

where

$$\tau^* \equiv \tau_c/(\mathrm{Be}). \tag{13}$$

The significance of S_0 is that for small values of y the reaction rate is approximately $yS_0(\xi)$. At $\xi_{\max}$, for small y the reaction rate is y/τ^*, and hence we take τ^* to be the characteristic reaction time scale. Note that the maximum reaction rate is $S_{\max} = 1/\tau_c = \mathrm{Be}/\tau^*$.

The values of the thermochemical parameters used in the simulations are summarized in Table 1.

3. GOVERNING EQUATIONS

The governing equations for the velocity $\mathbf{u}(\mathbf{x}, t)$, the mixture fraction $\xi(\mathbf{x}, t)$, and the perturbation $y(\mathbf{x}, t)$ are solved by a pseudo-spectral method on an N^3 grid. Periodic boundary conditions are applied so that all the fields are statistically homogeneous.

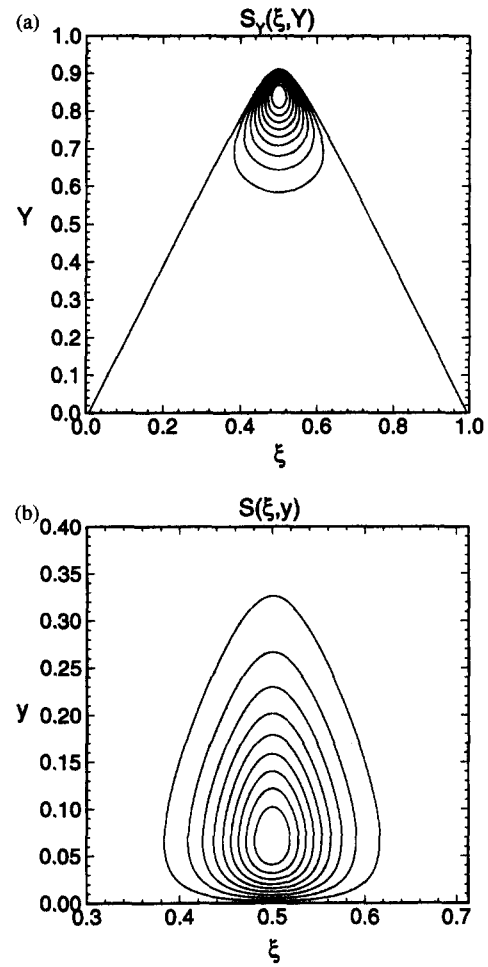

Fig. 5. Contour plots of the reaction rate in composition space $\xi_s = 0.5$, $K = 400$, $B = 15$, $\tau_c = 1$: (a) $S_Y(\xi, Y)$; (b) $S(\xi, y)$. Contour intervals are 0.1, with the innermost contour value being 0.9.

Because the density ($\rho = 1$) and the kinematic viscosity ν are constant, the evolution of the velocity field is unaffected by the ξ and y fields. The velocity field is solenoidal ($\nabla \cdot \mathbf{u} = 0$), and evolves according to the Navier–Stokes equations augmented by artificial forcing to yield statistically-stationary homogeneous nearly-isotropic turbulence. The way this is done, and the properties of the resulting turbulence, are fully described by Eswaran and Pope [14] and Yeung and Pope [13], and are summarized in the next section.

TABLE 1

Thermochemical Parameters

Specified Thermochemical Parameters	
ξ_s	0.5
K	400
B	15
τ^*	variable
Derived Thermochemical Parameters	
$\xi_{\max}$	0.5
ξ_l	0.384
ξ_r	0.616
$\Delta\xi_r$	0.232
$Y_{\max}$	0.909
τ_c	$\tau^* Be \approx 40.8\tau^*$
$S_{\max}$	$\tau_c^{-1} \approx 0.0245/\tau^*$

The evolution equation for the mixture fraction $\xi(\mathbf{x}, t)$ also contains forcing to maintain statistical stationarity. This is done in an indirect way, which is now described. Then the implied equation for $\xi(\mathbf{x}, t)$ is presented.

The equation

$$\frac{D}{Dt}\tilde{\xi} = \Gamma \nabla^2 \tilde{\xi} \tag{14}$$

is solved for the conserved passive scalar $\tilde{\xi}$. It is known that after some time $\tilde{\xi}$ becomes self-similar, with a one-point one-time distribution that is close to Gaussian [15].

We use square brackets [ ] to denote volume averages of fields. Thus the (time-dependent) volume average of $\tilde{\xi}(\mathbf{x}, t)$ is $[\tilde{\xi}]$ and the rms $\sigma_{\tilde{\xi}}$ is given by

$$\sigma_{\tilde{\xi}}^2 = \left[\left(\tilde{\xi} - [\tilde{\xi}]\right)^2\right]. \tag{15}$$

Then the quantity

$$\hat{\xi} = \left(\tilde{\xi} - [\tilde{\xi}]\right)/\sigma_{\tilde{\xi}}, \tag{16}$$

has volume average mean zero and variance unity. Based on this variable, the mixture fraction is defined by

$$\xi(\mathbf{x}, t) = \langle \xi \rangle + \xi' \hat{\xi}(\mathbf{x}, t), \tag{17}$$

where $\langle \xi \rangle$ and ξ' are the *specified* mean and standard deviation. Thus at all time the volume average mixture fraction is $\langle \xi \rangle$, and its rms is ξ'.

It can be deduced from the above, that the mixture fraction evolves by

$$\frac{D\xi}{Dt} = \Gamma \nabla^2 \xi + \frac{1}{2}(\xi - \langle \xi \rangle)[\chi]/\xi'^2, \tag{18}$$

where χ—the scalar dissipation—is defined by

$$\chi = 2\Gamma \nabla\xi \cdot \nabla\xi. \tag{19}$$

Thus, the final term in Eq. 18 corresponds to the artificial forcing. It may be observed that this is linear, deterministic forcing, with no specified parameters.

The equation solved for the reaction progress variable is

$$\frac{DY}{Dt} = \Gamma \nabla^2 Y + S_Y(\xi, Y) + \frac{1}{2} Y_e'(\xi)(\xi - \langle \xi \rangle)[\chi]/\xi'^2. \tag{20}$$

The four terms in the equation represent, respectively, the rate of change of Y following the fluid; molecular diffusion; chemical reaction; and, forcing. The rationale for the forcing term is given shortly.

From the definition of the perturbation, $y = Y_e(\xi) - Y$, we obtain

$$\frac{Dy}{Dt} = Y_e'(\xi)\frac{D\xi}{Dt} - \frac{DY}{Dt}. \tag{21}$$

Then, from Eqs. 18 and 20 we obtain

$$\frac{Dy}{Dt} = \Gamma \nabla^2 y - \frac{1}{2}\chi Y_e''(\xi) - S(\xi, y). \tag{22}$$

It may be seen, then, that the forcing term in the Y equation (Eq. 20) is specified to be $Y_e'(\xi)$ times that in the ξ equation (Eq. 18) so that (in Eq. 21) the forcing terms vanish. Hence the forcing has no effect on y. In particular, if the fluid is in equilibrium (i.e., $y = 0$) the forcing terms do not cause a departure from equilibrium.

In Eq. (22) the *mixing rate* Z $(\mathbf{x}, t)$, defined by

$$Z = -\tfrac{1}{2}\chi Y_e''(\xi), \tag{23}$$

is of central theoretical importance. It is non-negative, and hence tends to draw the fluid away from equilibrium (i.e., increasing y),

whereas the (nonnegative) reaction rate S tends to decrease y towards equilibrium.

4. SIMULATIONS

All the simulations performed have statistically-identical velocity fields, with a nominal Reynolds number of $R_\lambda = 17$. Four different values of $\xi^* = \xi'/\Delta\xi_r$ are considered, namely: 0.172, 0.517, 1.000, and 1.552. As described below, excellent spatial resolution is achieved by using 32^3, 64^3, 96^3, and 128^3 grid nodes, respectively, for the four cases. Most of the results from 32^3 and 64^3 calculations are obtained by averaging the results from 8 statistically identical and independent simulations.

4.1. Velocity

The velocity fields are marched in time using a variant of Rogallo's algorithm [16] to solve the incompressible Navier–Stokes equations with artificial forcing. Starting from some initial conditions, the velocity fields are advanced in time until a statistically stationary state is achieved. The details of the calculation procedure and the forcing scheme are fully described by Eswaran and Pope [14] and by Yeung and Pope [13]. The purpose of this subsection is to characterize the statistical properties of the resulting statistically stationary velocity fields.

Table 2 defines the input parameters and the primary statistics, and it gives their numerical values. The lowest wavenumber in the simulations k_0 is taken to be unity: correspondingly, the solution domain is a cube of side 2π. The physical input parameters are ν and the forcing parameters K_F, T_F, ϵ^*, and T_M^* (see Yeung and Pope [13] for definitions). The primary statistics (e.g., κ and ϵ) are volume-average quantities; and the values shown in the Table are time-averaged over the duration of the simulation.

Since the physical input parameters are the same for each simulation (and since the numerical errors are very small), the small differences in the resulting statistics (e.g., u' and l) are attributable to statistical variability. This variability appears to be an underappreciated feature of direct numerical simulations: it is normal practice to report the results of a single simulation. To illustrate the level of variability, Fig. 6 shows the evolutions of several statistics

TABLE 2

Summary of Velocity-Field Statistics[a]

N—grid size	N	32	64	96	128
N_s—number of simulations	N_s	8	8	1	1
ν—kinematic viscosity	ν	0.087	0.087	0.087	0.087
κ—turbulent kinetic energy	κ	1.642	1.579	1.473	1.459
ϵ—mean dissipation rate	ϵ	0.768	0.735	0.642	0.695
u'—turbulence intensity $(\frac{2}{3}\kappa)^{1/2}$	u'	1.046	1.026	0.991	0.986
l—longitudinal integral length scale	lk_0	1.930	1.962	2.092	1.985
λ—Taylor scale	λ/l	0.742	0.741	0.731	0.728
η—Kolmogorov scale	η/l	0.089	0.089	0.087	0.088
T_e—eddy turnover time (l/u')	T_e	1.885	1.960	2.191	2.038
τ_η = Kolmogorov time scale	τ_η/T_e	0.179	0.175	0.168	0.174
T—duration of simulation	T/T_e	16.995	12.261	9.141	1.423
$R_l \equiv u'l/\nu$	R_l	23.4	23.3	23.8	22.7
$R_\lambda \equiv u'\lambda/\nu$	R_λ	17.4	17.3	17.4	16.5
k_0—smallest wavenumber	$k_0\eta$	0.172	0.174	0.182	0.175
k_{max}—largest resolved wavenumber	$k_{max}\eta$	2.59	5.22	8.18	10.52
K_F—forcing parameter	K_F/k_0	$\sqrt{2}$	$\sqrt{2}$	$\sqrt{2}$	$\sqrt{2}$
T_F—forcing parameter	T_F	0.6369	0.6369	0.6369	0.6369
ϵ^* = forcing parameter	ϵ^*	0.01306	0.01306	0.01306	0.01306
T_m^* = forcing parameter	T_m^*	0.4	0.4	0.4	0.4

[a] Dimensional quantities (e.g., ν, κ, ϵ, T_e) are in arbitrary but consistent units.

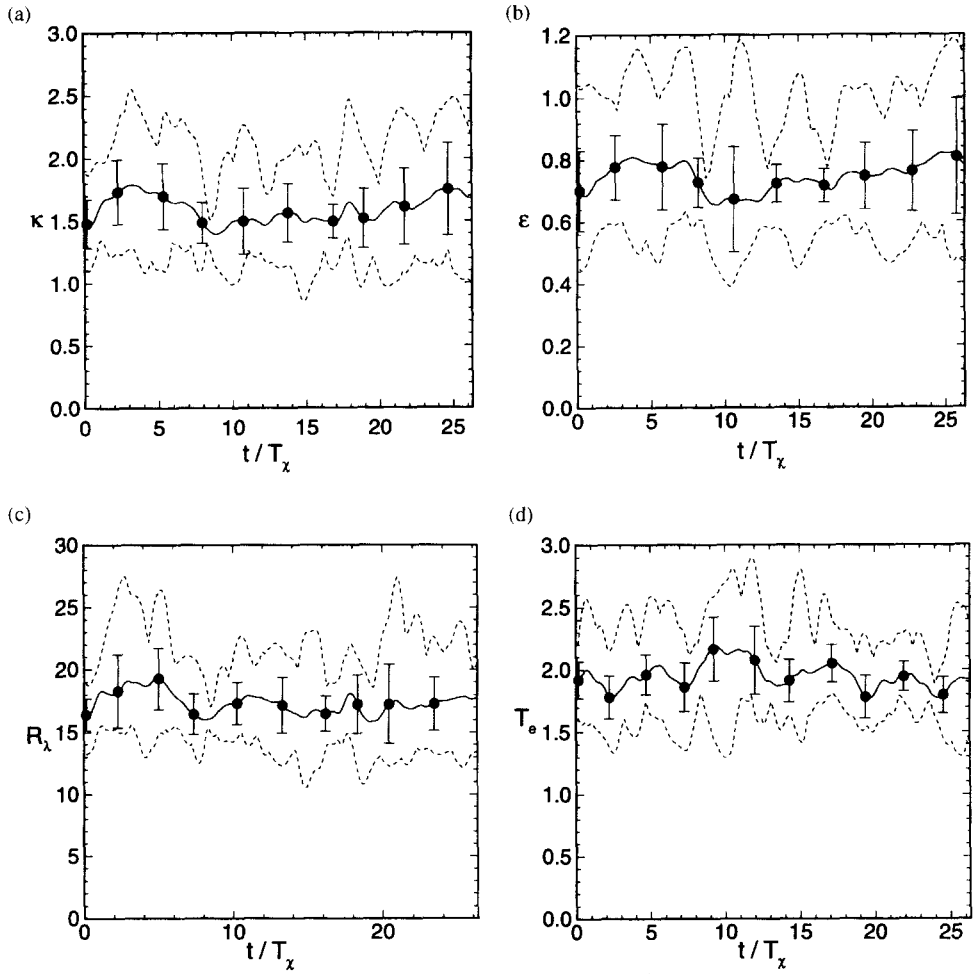

Fig. 6. Temporal evolution of statistics from 8 statistically identical 64^3 simulations: (a) kinetic energy, (b) dissipation, (c) Taylor-scale Reynolds number, (d) eddy turnover time. The dashed lines show the maximum and minimum of values from the eight simulations. The solid line is the mean, with the error bars denoting the 95% confidence intervals.

for the 8 statistically-identical 64^3 simulations. Variations of almost a factor of 4 may be observed in ϵ.

The quantity $k_{\max}\eta$ characterizes the spatial resolution of the velocity field. A rule of thumb is that $k_{\max}\eta \geq 1$ is adequate, and $k_{\max}\eta \geq 2$ is excellent [13]. Hence, as far as the velocity field is concerned, the spatial resolution is excellent (in fact, excessive).

4.2. Mixture Fraction

The mixture fraction equation (Eq. 14) is again solved by Rogallo's pseudo-spectral algorithm. Starting from an initial condition, after some time the mixture fraction field $\xi(\mathbf{x}, t)$ (as well as the velocity field) becomes statistically stationary. In this subsection, the primary statistics of these stationary field are reported. It should be appreciated that the standardized mixture fraction field $\hat{\xi}(\mathbf{x}, t)$—which have zero mean and unit variance (see Eqs. 15–17)—are statistically identical for all the simulations (independent of $\xi^* = \xi'/\Delta\xi_r$). (Of course both the ξ and $\hat{\xi}$ fields are independent of Da.)

Table 3 defines and summarizes the principal statistics. The time scale T_χ—which is used henceforth to nondimensionalize the time t—is the decay time scale of the (unforced) mixture fraction variance:

$$T_\chi \equiv \xi'^2/\langle \chi \rangle. \tag{24}$$

TABLE 3

Summary of Mixture Fraction Statistics

N—grid size	N	32	64	96	128
N_s—number of simulations	N_s	8	8	1	1
T_χ—scalar time scale ($\xi'^2/\langle\chi\rangle$)	T_χ/T_e	0.493	0.466	0.436	0.475
r = time scale ratio ($(\kappa/\epsilon)/T_\chi$)	r	2.302	2.350	2.422	2.172
$\mu_3(\hat{\xi})$—skewness of $\hat{\xi}$	$\mu_3(\hat{\xi})$	−0.025	0.116	−0.555	−0.383
$\mu_4(\xi)$—flatness of $\hat{\xi}$	$\mu_4(\hat{\xi})$	2.891	3.019	3.443	2.846
$\langle\hat{\theta}\rangle$—mean of $\hat{\theta} \equiv \ln(\chi/[\chi])$	$\langle\hat{\theta}\rangle$	−0.663	−0.664	−0.707	−0.625
$\sigma_{\hat{\theta}}^2$ = variance of $\hat{\theta}$	$\sigma_{\hat{\theta}}^2$	1.588	1.588	1.695	1.468
$\mu_3(\hat{\theta})$—skewness of $\hat{\theta}$	$\mu_3(\hat{\theta})$	−0.499	−0.496	−0.458	−0.467
$\mu_4(\hat{\theta})$—flatness of $\hat{\theta}$	$\mu_4(\hat{\theta})$	3.504	3.507	3.381	3.562
$\rho_{\hat{\xi}\hat{\theta}}$—correlation coefficient of $\hat{\xi}$ and $\hat{\theta}$	$\rho_{\hat{\xi}\hat{\theta}}$	−0.01	0.04	−0.223	−0.204
ξ^* = reaction zone (thickness parameter $\xi'/\Delta\xi_r$	ξ^*	0.172	0.517	1.000	1.552
ξ_B—scalar scale (Eq. 26)	$\xi_B/\Delta\xi_r$	0.104	0.318	0.632	0.938
l_r—reaction zone thickness (Eq. 28)	l_r/l	1.162	0.383	0.193	0.129
	l_r/η	12.999	4.311	2.221	1.458
	$k_0 l_r$	2.242	0.751	0.404	0.256
	$k_{\max} l_r$	33.63	22.54	18.17	15.36
Σ_s = area density of stoichiometric surface	$\Sigma_s\eta$	0.178	0.179	0.180	0.176
	$\Sigma_s l_r$	2.314	0.771	0.399	0.257
p_R—probability of $\xi_l \le \xi < \xi_r$	p_R	0.997	0.667	0.398	0.249
Z—mixing rate ($-\frac{1}{2}\chi Y_e''$)	$\langle Z\rangle T_\chi$	0.020	0.086	0.112	0.250

Recall that $\langle\chi\rangle \equiv \langle 2\Gamma\nabla\xi\cdot\nabla\xi\rangle$ is the mean scalar dissipation. The mechanical-to-scalar time scale ratio $r \approx 2.3$ agrees with that obtained by Eswaran and Pope [14] even though the Reynolds number here is smaller.

Table 3 and Fig. 7, show some of the marginal and joint statistics of $\hat{\xi}$ and of the logarithm of χ normalized by its volume average $[\chi]$:

$$\hat{\theta} \equiv \ln(\chi/[\chi]). \tag{25}$$

To a good approximation, at least up to three standard deviations, the pdf of $\hat{\xi}$, $f_\xi(\psi)$, is Gaussian. In the central region, the pdf of $\hat{\theta}$, $f_\theta(\theta)$ is also approximately Gaussian, but clearly the tails are not, with the negative tail being exponential and leading to a significant negative skewness.

To the statistical precision of the results, it appears that $\hat{\xi}$ and $\hat{\theta}$ are independent. While the single 96^3 and 128^3 runs show the correlation coefficient between $\hat{\xi}$ and $\hat{\theta}$ to be of order -0.2, it is nevertheless clear from Fig. 7c that this is almost certainly due to statistical variability.

Figure 8 shows the conditionally averaged scalar dissipation. If ξ and χ were independent, then $\langle\chi|\hat{\xi}\rangle/\langle\chi\rangle$ would be unity, independent of $\hat{\xi}$. Given the size of the confidence intervals in Fig. 8, and recalling that $\langle\chi|\hat{\xi}\rangle$ is statistically-symmetric about $\hat{\xi} = 0$ the results are not inconsistent with independence (i.e., $\langle\chi|\xi\rangle = \langle\chi\rangle$).

The statistics described so far (i.e. down to $\rho_{\hat{\xi}\hat{\theta}}$ in Table 3) are independent of ξ^*. Hence, different values for different simulations reflect statistical variability.

We use the parameter $\xi^* \equiv \xi'/\Delta\xi_r$ as the non-dimensional measure of the reaction zone thickness—or, rather, the reaction zone thinness, since $\Delta\xi_r$ various inversely with ξ^*. Bilger [2] argues that, in place of ξ', the physically appropriate scale to use is the *scalar-scale*

$$\xi_B \equiv \left(\langle\chi\rangle/(\epsilon/\nu)^{1/2}\right)^{1/2}. \tag{26}$$

This is the microscale, of dimension ξ, analogous to the Kolmogorov velocity scale, introduced by Gibson [17]. It may be seen from Table 3 that the range of ξ^* considered goes from $\xi^* = 0.172$ (corresponding to $\Delta\xi_r \approx 10\xi_B$) to $\xi^* = 1.552$ (corresponding to $\Delta\xi_r \approx \xi_B$). (As is discussed in the next subsection,

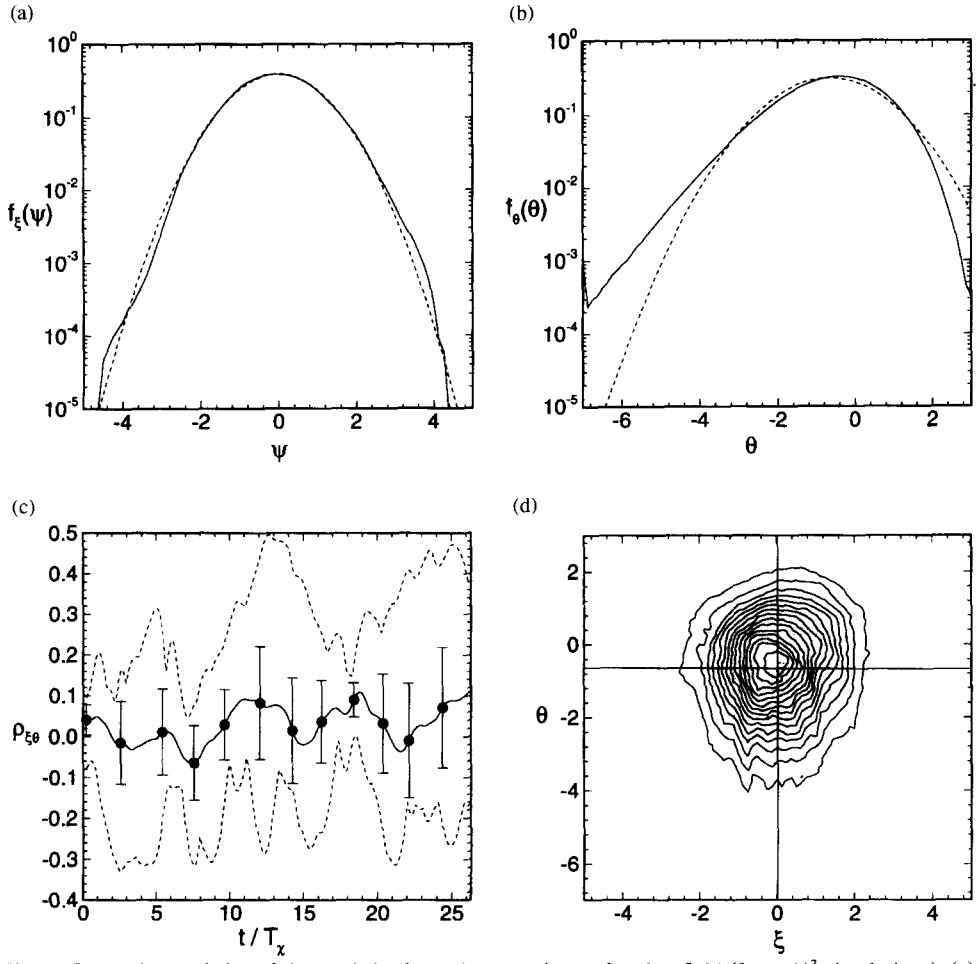

Fig. 7. One-point statistics of the statistically stationary mixture fraction field (from 64^3 simulations). (a) marginal pdf of the standardized mixture fraction $\hat{\xi}$. (b) marginal pdf of the normalized logarithm of scalar dissipation $\hat{\theta}$ (Eq. 25). (c) correlation coefficient between $\hat{\xi}$ and $\hat{\theta}$. (d) joint pdf of $\hat{\xi}$ and $\hat{\theta}$.

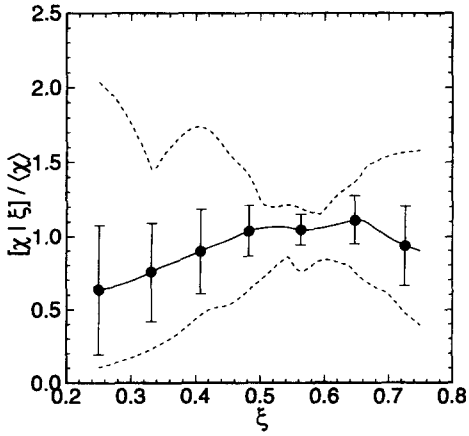

Fig. 8. Conditional mean of the scalar dissipation from 64^3 simulations. Significance of lines—same as Fig. 6.

larger grid sizes, or lower R_λ, is needed for resolved simulations at larger values of ξ^*.)

Several other statistics are now described which provide more insight into the significance of ξ^*.

We define p_R to be the probability that ξ is in the reaction zone in mixture-fraction space. That is,

$$p_R \equiv \text{Prob}\{\xi_l \le \xi < \xi_r\}$$

$$= \int_{\xi_l}^{\xi_r} f_\xi(\psi)\, d\psi, \tag{27}$$

where $f_\xi(\psi)$ is the pdf of ξ. It may be seen that p_R is very close to unity at $\xi^* = 0.172$ and decreases to about 1/4 at $\xi^* = 1.552$.

A characteristic length scale of the reaction zones is taken to be

$$l_r \equiv \Delta\xi_r/(\nabla\xi \cdot \nabla\xi)^{1/2}. \quad (28)$$

The ratios l_r/l and l_r/η are given in Table 3. At the largest value of ξ^*, l_r is about $1\frac{1}{2}\eta$: but is should be recalled that η underestimates by about an order of magnitude the characteristic scale of the smallest features of the velocity field [18], [19].

The surface-to-volume ratio (or area density) of the iso-scalar surface $\xi(\mathbf{x}, t) = \psi$ is denoted by $\Sigma(\psi)$. It can be evaluated from the geometric equation [20]

$$\Sigma(\psi) = f_\xi(\psi)\langle|\nabla\xi| \,|\, \xi = \psi\rangle. \quad (29)$$

For the stoichiometric surface, we write $\Sigma_s = \Sigma(\xi_s)$, and values of Σ_s are given in Table 3.

For a small length l^*, the product $\Sigma_s l^*$ is the fraction of the volume occupied by a sheet of thickness l^* that straddles the stoichiometric surface. It may be observed from Table 3 that, as expected from the above argument, for the smaller values of l_r, the product $\Sigma_s l_r$ gives the volume fraction (i.e., probability) of fluid in the reaction zone, p_R.

4.3. Perturbation

The equation for the perturbation $y(\mathbf{x}, t)$ (Eq. 22) is solved by the same pseudo-spectral method used for $\mathbf{u}$ and ξ. In addition to convection and diffusion, this equation contains source terms due to mixing ($Z = -\frac{1}{2}\chi Y_e''(\xi)$) and to reaction, $S(\xi, y)$. In order for the simulations to be accurate, the Z and S fields must be well resolved on the computational grid. For a given mixture fraction field ξ, if $\Delta\xi_r$ is decreased, the length scale of the Z field decreases, and hence the resolution requirements increase.

These resolution requirements are studied in detail by Lee [21], who performed extensive numerical tests. The minimum grid size $N_{\min}$ that yields adequate resolution depends on R_λ, ξ^*, and the details of the forcing. With the forcing used here, an approximate empirical expression obtained by Lee [21] becomes

$$N_{\min} = (0.404 + 2.165\xi^*)R_\lambda^{1.2}. \quad (30)$$

Evidently, for $\xi^* = 1$ (because of the thin reaction zones) the required value of N is 6 times that required to resolve the velocity field alone (i.e., $\xi^* = 0$). Since the computer time required scales approximately as N^4, it is clearly very costly to perform simulations with large ξ^*.

A contour plot of $N_{\min}$ given by Eq. 30 is shown on Fig. 9. It may be seen that, according to this guideline, the four values of ξ^* chosen in the present work lead to well-resolved simulations on the four grid sizes employed. In each case, the tail of the spectrum of y was examined to confirm that indeed the field is well resolved.

All the simulations reported start at time $t = 0$ with statistically-stationary velocity and mixture fraction fields, and with the initial condition $y(\mathbf{x}, 0) = 0$ corresponding to chemical equilibrium.

5. GLOBAL EXTINCTION

The starting point for understanding the simulation results (shortly to be presented) is the volume average of the evolution equation for the perturbation $y(\mathbf{x}, t)$ (Eq. 22):

$$\frac{d[y]}{dt} = [Z] - [S]. \quad (31)$$

Recall that square brackets denote the volume average, and that the mixing rate is $Z =$

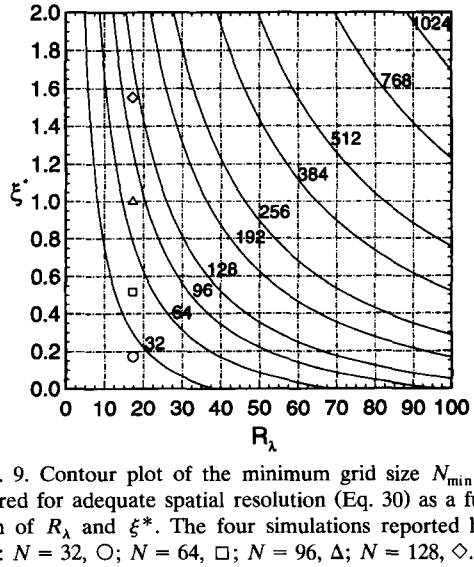

Fig. 9. Contour plot of the minimum grid size $N_{\min}$ required for adequate spatial resolution (Eq. 30) as a function of R_λ and ξ^*. The four simulations reported here are: $N = 32$, ○; $N = 64$, □; $N = 96$, △; $N = 128$, ◇.

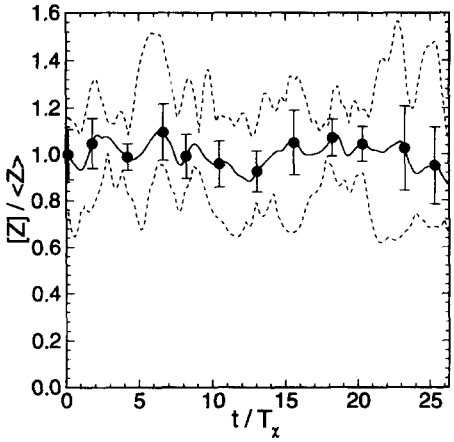

Fig. 10. Normalized mixing rate versus time for $R_\lambda = 17.3$, $\xi^* = 0.517$. Dashed lines show maximum and minimum of the eight simulations. The solid line and error bars show the mean and 95% confidence interval.

$-\frac{1}{2}\chi Y_e''(\xi)$. When Eq. 22 is volume averaged, the transport terms (convection and diffusion) vanish because of periodicity.

For given values of R_λ and ξ^*, the mixing rate $[Z]$ is a statistically stationary function of time, independent of Da. Figure 10 shows $[Z]$ (normalized by its time average, $\langle Z \rangle$) as a function of time for $R_\lambda = 17.3$ and $\xi^* = 0.517$. This illustrates the stationarity of $[Z]$ and the level of statistical variability. Values of $\langle Z \rangle$ are given in Table 3.

At sufficiently large Da there is stable combustion. In this case $[y]$ is statistically stationary; and (on average) reaction $[S]$ balances mixing $[Z]$. results from such a case ($R_\lambda = 17.3$, $\xi^* = 0.517$, Da = 93.2) are shown on Fig. 11. The imbalance between reaction and mixing is quantified by the nondimensional quantity

$$\epsilon_S(t) \equiv ([S] - [Z])/[Z]. \tag{32}$$

It may be seen from Eq. 31 and Fig. 11c that for this case of stable combustion the mean $\langle \epsilon_S \rangle$ is zero.

(Because of the initial condition $y(\mathbf{x}, 0) = 0$, both $[y]$ and $[S]$ are initially zero, and ϵ_S equals -1. There is then a short initial transient during which these quantities rise to their stationary values. While this transient is perfectly well resolved in the simulations, the output-time increments used to generate Fig. 11 are too large to reveal the transient.)

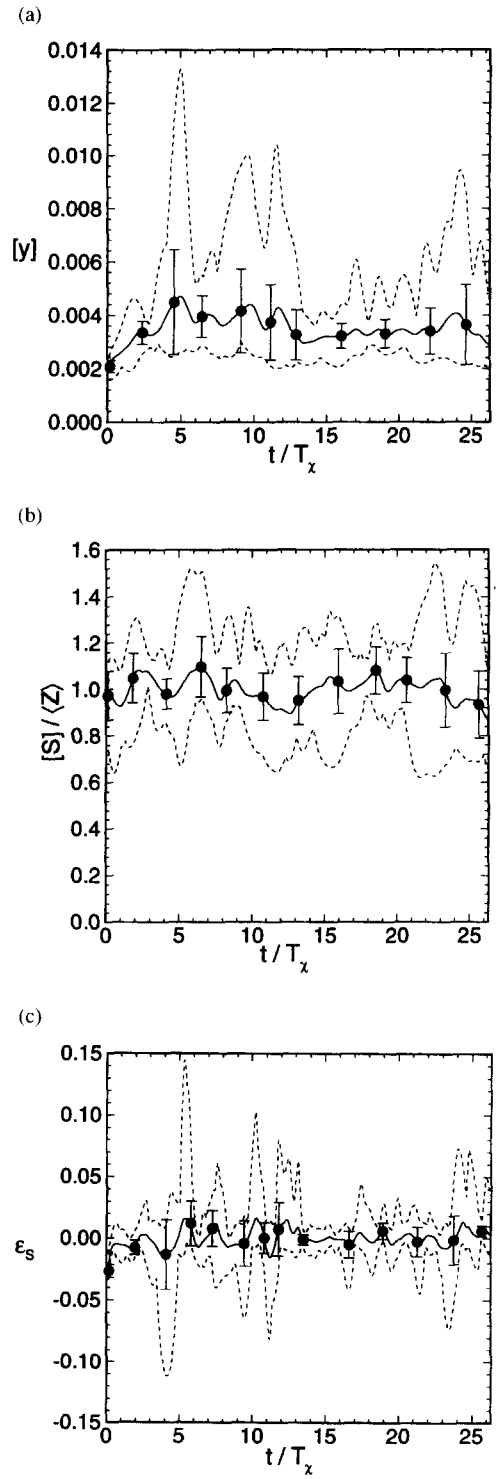

Fig. 11. Volume-averaged quantities versus time for stable combustion ($R_\lambda = 17.3$, $\xi^* = 0.517$, Da = 93.2) (a) mean perturbation, (b) mean reaction rate, (c) imbalance index (Eq. 32). Significance of lines—same as Fig. 10.

At the other extreme, for zero Damkohler number the reaction rate $[S]$ is zero. Hence Eq. 31 shows that $[y]$ increases monotonically with time—there is no statistically stationary state. For this case ϵ_S is -1 (Eq. 32).

Figure 12 shows results for a carefully selected intermediate value of Damkohler number (Da = 18.6). By the end of these long simulations ($t \approx 26T_\chi$) it may be seen that in four of the eight simulations global extinction has occurred (i.e., $\epsilon_S = -1$). There is every reason to suppose that the other four simulations would also have exhibited global extinction if the runs had been extended for long enough. Note also, that if the runs had terminated at $t = 12T_\chi$, the conclusions drawn would have been unclear or possibly erroneous: in the time interval $0 < t < 12T_\chi$, the confidence intervals on ϵ_S straddle zero, consistent with stable combustion.

As well as illustrating global extinction, these results reveal that—because of statistical variability—there are inherent difficulties in quantifying the phenomenon. For given parameters $(R_\lambda, \xi^*, \mathrm{Da})$ does global extinction occur? In the absence of statistical variability (e.g., for a laminar system), the question can be answered: yes, if $\mathrm{Da} < \mathrm{Da}_{\mathrm{crit}}$; no, if $\mathrm{Da} > \mathrm{Da}_{\mathrm{crit}}$. And the phenomenon is then quantified by determining the critical Damkohler number, $\mathrm{Da}_{\mathrm{crit}}$.

But with statistical variability, the question can only be answered probabilistically, and the duration of the simulation T is an additional parameter. For example, two possible ways to quantify the phenomenon are:

i. the probability of extinction by the normalized time $\hat{T}$

$$P_E\left(\hat{T}, R_\lambda, \xi^*, \mathrm{Da}\right) \equiv \mathrm{Prob}\{\epsilon_S(T) < -0.99\},$$

where $\hat{T} = T/T_\chi$.

ii. the normalized mean time to extinction $\hat{T}_E(R_\lambda, \xi^*\ \mathrm{Da})$, defined as the expectation of the earliest normalized time t/T_χ at which ϵ_S equals the threshold value -0.99. (For surely-stable combustion $\hat{T}_E$ is infinite.)

The amount of computer time required to "measure" P_E or $\hat{T}_E$ to useful precision is unthinkably vast.

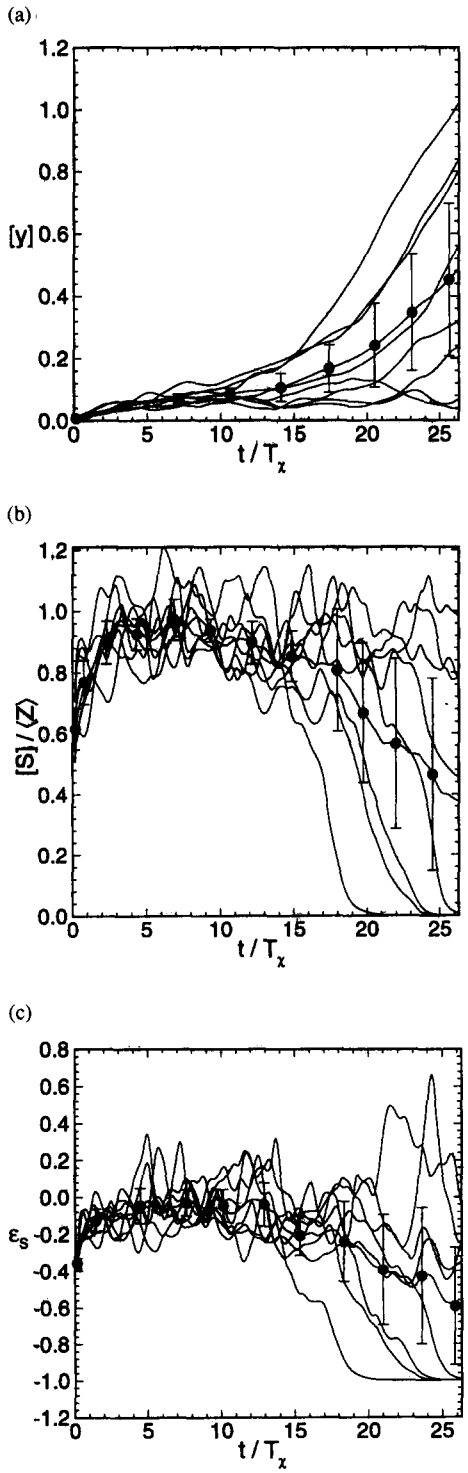

Fig. 12. Volume-averaged quantities versus time for simulations exhibiting global extinction ($R_\lambda = 17.3$, $\xi^* = 0.517$, Da = 18.6). Line with symbols and error bars—mean over eight simulation and 95% confidence interval. Other lines —from each of the eight simulations. (a) mean perturbation, (b) mean reaction rate, (c) imbalance index.

Given the practical impossibility of precisely quantifying the extinction phenomenon, we content ourselves with estimating an imprecisely defined Damkohler number range to characterize extinction. The lower and upper bounds of this range Da_l and Da_u (which depend on R_λ and ξ^*) are such that in a simulation of duration of order 30 T_χ, say, global extinction is likely for $Da < Da_l$, but is unlikely for $Da > Da_u$.

In order to estimate the extinction range (Da_l, Da_u), rather than performing many simulations with different values of Da, it is computationally more efficient to perform a single simulation in which Da is gradually reduced (by increasing τ_c) until extinction occurs. For each value of ξ^* studied, such simulations were performed with Da decreasing according to

$$Da(t) = Da_0 \exp(-t/T_0), \tag{33}$$

where the values of Da_0 and T_0 are given in Table 4. Figure 13 shows the imbalance index ϵ_S obtained from these simulations, plotted against $Da(t)$. Notice that $Da(t)$ decreases (corresponding to time increasing) from left to right in these figures.

It may be seen from Fig. 13 that the initial Damkohler number, Da_0, is chosen to be sufficiently large so that ϵ_S is very close to zero for a substantial initial period, corresponding to stable combustion. And the duration of the simulations is sufficiently long so that ϵ_S approaches -1, corresponding to global extinction. Based on these curves, the values of Da_l and Da_u are subjectively ascribed: their values are given in Table 4 and are indicated on Fig. 13.

(It may be noted that, in Table 4, T_0/τ_l^* gives the decay time scale of $Da(t)$ relative to the reaction time scale τ^* at $Da = Da_l$. Clearly $Da(t)$ decays very slowly compared to the reaction time scale, and hence—as far as the local balance between reaction and mixing is concerned—the decay of Da is quasi-static.)

Figure 14 shows the extinction ranges (Da_l, Da_u) determined from the simulation on the $Da - \xi^*$ parameter plane. Also shown are the values of Da_{crit} given by different theories —presented in the next section. In spite of the imprecisions in the definition and determination of the extinction range, it is nevertheless clear that, in the simulations, extinction occurs at a significantly higher Damkohler number than predicted by the theories.

6. MODELS OF NONPREMIXED COMBUSTION

Most can be learned from simulations when the results are compared with the predictions of theories or models. In this section we outline the application of four simple models in the present context. Their predictions of extinction are compared to the results presented in the previous section: and further comparisons are given in Section 7.

6.1. Flamelet Model

The fundamental assumption in the flamelet model (see, e.g., Peters [3]) is that the structure of the turbulent flame is locally the same as that of a strained laminar flame. A first step, then, in the application of the flamelet model is to determine properties of the strained lami-

TABLE 4

Global Extinction Parameters

N—grid size	N	32	64	96	128
N_s—number of simulations	N_s	8	8	1	1
$\xi^* = \xi'/\Delta\xi_r$	ξ^*	0.172	0.517	1.000	1.552
Da_0—initial value of Da (Eq. 33)	Da_0	47.4	372.8	1299.2	2467.1
T_0—decay time scale (Eq. 33)	T_0/T_χ	20.147	3.677	2.699	1.759
τ_l^*—reaction time scale for $Da = Da_l$	T_0/τ_l^*	24.	74.	351.	704
Da_l—lower value of extinction range		1.2	20.	130.	400.
Da_u—upper value of extinction range		3.	60.	300.	500.

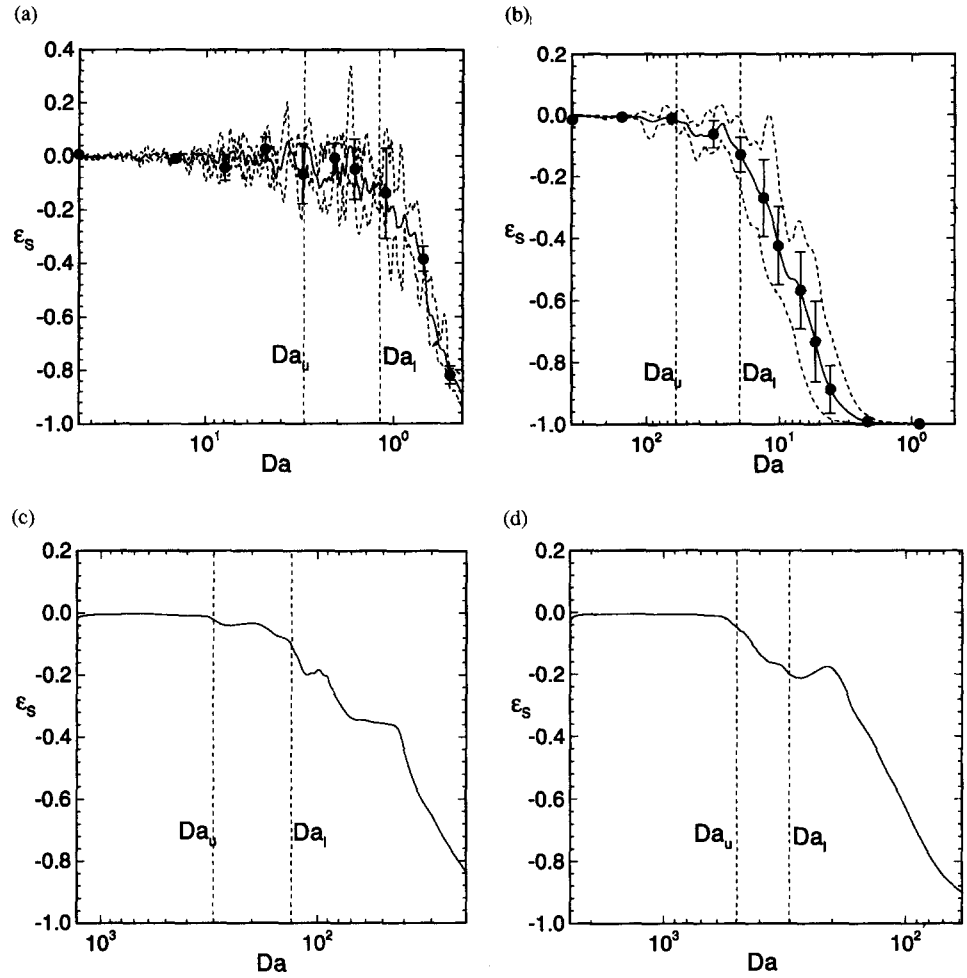

Fig. 13. Imbalance index ϵ_S (Eq. 32) against Damkohler number for simulations in which Da is gradually decreased with time. (a) $\xi^* = 0.172$, (b) $\xi^* = 0.517$, (c) $\xi^* = 1.000$, (d) $\xi^* = 1.552$. In (a) and (b), the dashed lines are the maximum and minimum over the 8 runs performed, and the line and error bars are the mean and 95% confidence interval.

nar flames. With the thermochemistry considered here, this is achieved by solving the conservation equations for ξ and Y, with a velocity field corresponding to uniform plane strain (with strain rate a). These equations (obtained from Eqs. 18 and 20 by omitting the forcing terms and assuming steady one-dimensional solutions $\xi(x)$ and $Y(x)$) are

$$\Gamma\frac{d^2\xi}{dx^2} + ax\frac{d\xi}{dx} = 0, \tag{34}$$

$$S_Y(\xi, Y) + \Gamma\frac{d^2Y}{dx^2} + ax\frac{dY}{dx} = 0, \tag{35}$$

and the appropriate boundary conditions are $\xi(-\infty) = Y(-\infty) = Y(\infty) = 0$, and $\xi(\infty) = 1$.

Equation 34 is solved analytically; and from the solution it is deduced that the scalar dissipation χ_s at stoichiometric (i.e., where $\xi(x) = \xi_s = 0.5$) is

$$\chi_s = a/\pi. \tag{36}$$

Thus either a or χ_s can be used to parametrize the strain rate.

As is well known (see, e.g., Giovangigli and Smooke [22]), equations of the form of Eq. 35 admit no solutions above a critical value of the strain rate, a_q; while for a value less than a_q,

there are two solutions—one stable and one unstable. In order to obtain these solutions and to determine a_q accurately, Equation 35 is solved numerically using arc-length continuation [23]: the details are given in Lee [21]. The value of a_q obtained is

$$a_q\tau^* = 5.312 \times 10^{-3}, \tag{37}$$

or, equivalently, the corresponding quenching value of the scalar dissipation is

$$\chi_F\tau^* = a_q\tau^*/\pi = 1.691 \times 10^{-3}. \tag{38}$$

The value of the perturbation $y = Y_e(\xi) - Y$ obtained from the strained laminar flame calculations can be parametrized by ξ and χ_s and is denoted by $y_F(\xi, \chi_s)$. Figure 15 shows y_F against ξ for $\chi_s/\chi_F = \frac{1}{3}, \frac{2}{3}$, and 1. In the next Section, the flamelet predication $y_F(\xi, \chi_s)$ of the perturbation y is compared with the DNS results. But now we return to the question of extinction.

In the flamelet model applied to turbulent nonpremixed combustion, if at a particular location on the stoichiometric surface the scalar dissipation rate χ exceeds χ_F, then it is assumed that there is local extinction of the

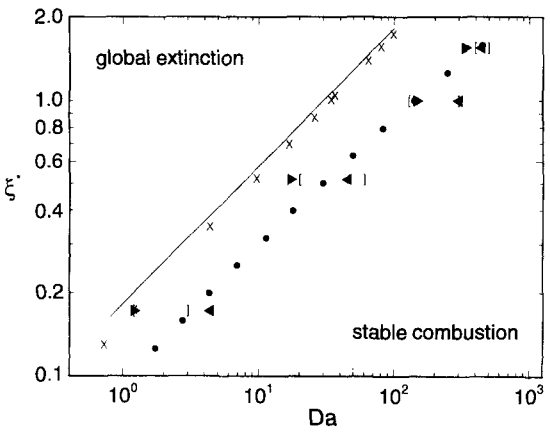

Fig. 14. The Da–ξ^* parameter plane showing extinction observations and predictions. Extinction range (Da_l, Da_u) determined from simulations: Da_l – [; Da_u –]. Critical Damkohler number $Da_{crit}(\xi^*)$ from the flamelet model—solid line; $Da_{crit}(\xi^*)$ from CMC—crosses; $Da_{crit}(\xi^*)$ from statistical model (Section 6.4)—solid circles. Triangles show $Da_{0.1}(\xi^*)$, ◁, and $Da_{0.5}(\xi^*)$, ▷, the values of Da at which the error in the flamelet model δ_F is 0.1 and 0.5, respectively (see Section 8).

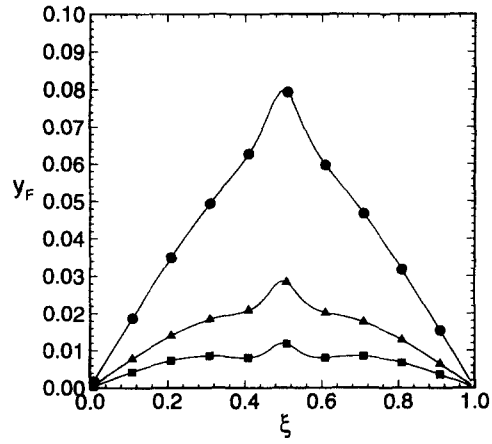

Fig. 15. Perturbation $y_F(\xi, \chi_s)$ obtained from the laminar flamelet model, with $\chi_s/\chi_F = \frac{1}{3}(\square), \frac{2}{3}(\triangle), 1(\bullet)$.

flame. Peters and Williams [24] define the fraction of burnable flamelets by

$$P_b = \text{Prob}\{\chi < \chi_F | \xi = \xi_s\} = \text{Prob}\{\chi/\chi_F < 1 | \xi = \xi_s\} \tag{39}$$

and they argue that global extinction occurs when P_b decreases below a critical value $P_{b,\text{crit}} = 0.72$. In the present context, P_b is determined by the parameters of the simulation, i.e., $P_b = P_b(\text{Da}, \xi^*)$ (at fixed R_λ). Hence this argument leads to a prediction of the critical Damkohler number $Da_{crit}(\xi^*)$. Specifically, on the Da–ξ^* plane, the line $Da_{crit}(\xi^*)$ is the locus of the points satisfying $P_b(\text{Da}, \xi^*) = P_{b,\text{crit}}$, and hence is determined implicitly by the equation

$$P_b(Da_{crit}(\xi^*), \xi^*) = P_{b,\text{crit}}. \tag{40}$$

The flamelet model prediction of $Da_{crit}(\xi^*)$ obtained from Eq. 40 is shown on Fig. 14. It may be seen that it underestimates the value of Da required for stable combustion by as much as a factor of 4. Furthermore, on the log-log plot, the slope of the $Da_{crit}(\xi^*)$ line is different from that given by the DNS data. It is readily shown that $Da_{crit}(\xi^*)$ obtained from Eq. 40 varies as $(\xi^*)^2$, whereas the dependence suggested by DNS data is $(\xi^*)^{2.32}$.

6.2. Conditional Moment Closure

We now apply the conditional moment closure (CMC) developed by Bilger [7] and Klimenko

[8] in the present context for the case of statistically stationary stable combustion.

The fundamental quantity of interest is the conditional mean of the reaction progress variable Y—conditioned, that is, on the value of the mixture fraction ξ. We introduce ζ as the sample-space variable corresponding to ξ. Then the conditional mean $Y_M(\zeta)$ is defined by

$$Y_M(\zeta) = \langle Y(\mathbf{x},t) | \xi(\mathbf{x},t) = \zeta \rangle. \tag{41}$$

Notice that ζ is an independent variable: and, because of the assumed statistical homogeneity and stationarity, Y_M does to depend on $\mathbf{x}$ or t. The simplest assumption that can be made in order to obtain the CMC equations is that fluctuations of $Y(\mathbf{x},t)$ from the conditional mean $Y_M(\xi(\mathbf{x},t))$ are negligibly small. Hence, fluctuations in $Y(\mathbf{x},t)$ are (by assumption) due entirely to fluctuations in ξ. While the assumption of zero conditional fluctuations is sufficient to obtain the CMC equations, it appears that weaker assumptions may suffice [25, 26].

Following Bilger's methodology, an ordinary differential equation for $Y_M(\zeta)$ is obtained from the evolution equation for Y, Eq. 20:

$$S_Y(\zeta, Y_M) + \frac{1}{2}\langle \chi \rangle \frac{d^2 Y_M}{d\zeta^2} + \frac{1}{2}\langle \chi \rangle (\zeta - \langle \xi \rangle) \times \left(Y_e'(\zeta) - \frac{dY_M}{d\zeta} \right) \Big/ \xi'^2 = 0. \tag{42}$$

The only assumptions made in obtaining this equation are that χ and ξ are statistically independent, and that fluctuations of Y about its conditional mean are negligible. The appropriate boundary conditions are $Y_M(0) = Y_M(1) = 0$.

The CMC equation (Eq. 42) is very similar to the laminar flame equation (Eq. 35), and the qualitative behavior of its solutions is the same. In particular, solutions exist only for a limited range of parameter values. This can be better understood if Eq. 42 is recast in the nondimensional form

$$2\,\mathrm{Da}\,\hat{S}_Y(\zeta, Y_M) + (\Delta\xi_r \xi^*)^2 \frac{d^2 Y_M}{d\zeta^2} + (\zeta - \langle \xi \rangle)\left(Y_e'(\zeta) - \frac{dY_M}{d\zeta} \right) = 0, \tag{43}$$

where the nondimensional reaction rate $\hat{S}_Y = S_Y \tau^*$ is independent of Da and ξ^*.

For given ξ^*, there is a critical value of Da, $\mathrm{Da}_{\mathrm{crit}}(\xi^*)$, below which Eq. (43) admits no solutions; while for $\mathrm{Da} > \mathrm{Da}_{\mathrm{crit}}$ there is a stable and an unstable solution.

For several values of ξ^*, Eq. 43 was solved numerically using arclength continuation to determine $\mathrm{Da}_{\mathrm{crit}}(\xi^*)$—the CMC prediction of the global extinction boundary. The values, plotted on Fig. 14, are quite close to the flamelet model prediction, and differ significantly from the DNS results.

It may be observed that for large Da and ξ^*, the first two terms in Eq. 43 must balance, and hence $\mathrm{Da}_{\mathrm{crit}}(\xi^*)$ scales as ξ^{*2}—as in the flamelet model. And for the same reason, for large ξ^*, the solution $Y_M(\zeta)$ depends on $\mathrm{Da}/\mathrm{Da}_{\mathrm{crit}}$, but only weakly on ξ^*. Figure 16 shows the perturbation from equilibrium

$$y_M(\zeta) \equiv Y_e(\zeta) - Y_M(\zeta), \tag{44}$$

obtained from Eq. (43) for $\xi^* = 1.552$ and $\mathrm{Da}_{\mathrm{crit}}/\mathrm{Da} = \frac{1}{3}, \frac{2}{3}$, and 1. Not surprisingly, these curves are similar to those obtained from the flamelet model (Fig. 15).

6.3. Quasi-Equilibrium Distributed Reaction

The third simple model considered is that of quasi-equilibrium distributed reaction (QEDR) introduced by Bilger [6].

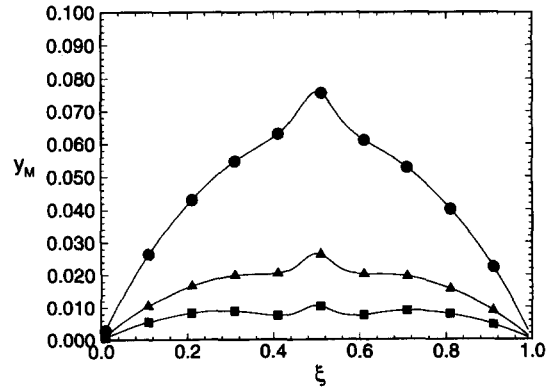

Fig. 16. Perturbations $y_M(\xi)$ obtained from the conditional moment closure with $\xi^* = 1.552$, $\mathrm{Da}_{\mathrm{crit}}/\mathrm{Da} = \frac{1}{3}(\square), \frac{2}{3}(\triangle), 1(\bullet)$. ($\mathrm{Da}_{\mathrm{crit}} = 80.4$).

The transport equation for the perturbation $y(\mathbf{x}, t)$ (Eq. 22) contains four terms—convection, diffusion, mixing and reaction. Bilger [6] argues that at high Da, and for mixture fractions in the reaction zone (i.e., $\xi_l < \xi < \xi_r$), there is a local balance between mixing and reaction. This leads to the QEDR prediction of y, denoted by $y_Q(\xi, \chi)$: by equating reaction and mixing, we obtain the implicit equation for y_Q

$$S\big(\xi, y_Q(\xi, \chi)\big) = -\tfrac{1}{2}\chi Y_e''(\xi). \tag{45}$$

The QEDR model leads then to an algebraic equation for the predicted perturbation, whereas the previous two models considered (flamelet and CMC) resulted in ordinary differential equations. Nevertheless the qualitative nature of the solutions is similar. With all other parameters fixed, there is an upper value of χ—denoted by χ_Q—for which Eq. 45 admits solutions. For χ less than χ_Q, there is a stable and an unstable solution. The value of χ_Q is obtained from Eq. 45 by substituting $S(\xi, y) = f(y)g(\xi)/\tau_c$, and taking the upper limit of $f(y)$, which is unity. After some manipulation the result is

$$\frac{\chi_Q}{\langle \chi \rangle} = \frac{\mathrm{Da}}{(\xi^*)^2}\left[\frac{-2g(\xi)}{Be\,\Delta\xi_r^{\,2}\,Y_e''(\xi)}\right]. \tag{46}$$

The QEDR model shows that a local balance between reaction and mixing is not possible if χ exceeds χ_Q. A reasonable extension of the theory, then, is to predict that global extinction occurs if

$$p_Q \equiv \mathrm{Prob}\{\chi > \chi_Q | \xi_l < \xi < \xi_r\}. \tag{47}$$

exceeds a critical value $p_{Q,\mathrm{crit}}$. It is readily shown from Eq. 46 that such a theory predicts that the critical Damkohler number $\mathrm{Da}_{\mathrm{crit}}$ scales with ξ^{*2}. This prediction is qualitatively the same as that of the flamelet and CMC models, and is at variance with the DNS observations.

6.4. Temporal Fluctuations in Volume Averages

As observed above, the three different models considered all predict that that the critical Damkohler number $\mathrm{Da}_{\mathrm{crit}}$ varies as $(\xi^*)^2$, whereas the DNS results suggest a scaling of $(\xi^*)^{2.3}$. At the highest value of ξ^* studied, the DNS extinction range $(\mathrm{Da}_l, \mathrm{Da}_u)$ is about 4 times greater than the value of $\mathrm{Da}_{\mathrm{crit}}$ given by the flamelet and CMC models. It is certainly true that the CMC and QEDR models have been used beyond their limits of validity; but nevertheless the discrepancy between all the models and the DNS observations requires further comment.

A possible explanation for this discrepancy lies in the significant temporal fluctuations in volume-averaged statistics in the simulations. Consider, for example, $\bar{p}_Q(t)$ defined as the *volume fraction* of the fluid in the reaction zone $(\xi_l < \xi < \xi_r)$ for which χ exceeds χ_Q. Thus $\bar{p}_Q(t)$ and p_Q (Eq. 47) are defined by the same event $\{\chi > \chi_Q | \xi_l < \xi < \xi_r\}$, but $\bar{p}_Q(t)$ is a volume average, rather than the probability. (The mean $\langle \bar{p}_Q(t) \rangle$ equals p_Q.)

At any time t in a simulation, it is reasonable to suppose that the current value of $\bar{p}_Q(t)$ is a better indicator of the propensity for global extinction that is the mean p_Q. And if the condition $\bar{p}_Q(t) > p_{Q,\mathrm{crit}}$ is taken as a predictor for global extinction, then clearly the fluctuations in $\bar{p}_Q$, not just its mean p_Q, affect extinction. In the present simulations, the fluctuations in $\bar{p}_Q(t)$ clearly increase with ξ^*, simply because the probability of fluid in the reaction zone ($p_R \equiv \mathrm{Prob}\{\xi_l < \xi < \xi_r\}$) decreases with increasing ξ^* (see Table 3). Hence, relative to the prediction based on the mean p_Q, the extinction prediction $\mathrm{Da}_{\mathrm{crit}}(\xi^*)$ based on $\bar{p}_Q(t)$ will increase more rapidly with ξ^*—more rapidly, therefore, than ξ^{*2}, in accord with the observation from DNS.

We now present a crude statistical model to demonstrate the plausibility of the above arguments. The central idea is to use averages over a finite ensemble of N random samples to simulate volume averages. The statistical fluctuations in the ensemble averages (which scale as $N^{-1/2}$) mimic the fluctuations in volume averages.

Random samples of mixture fraction, $\xi^{(n)}$, and of scalar dissipation, $\chi^{(n)}$, are drawn from Gaussian and log-normal distributions, respectively, with means and variances taken from Table 3. For the nth sample, the mixing rate is

$$Z^{(n)} = -\tfrac{1}{2}\chi^{(n)} Y_e''(\xi^{(n)}). \tag{48}$$

For a given value of ξ, the maximum reaction rate is $S_{max}(\xi) = g(\xi)/\tau_c$ (see Eq. 8). The reaction rate for the nth sample is modeled as

$$S^{(n)} = S_{max}(\xi^{(n)}), \quad \text{if } S_{max}(\xi^{(n)}) > Z^{(n)},$$
$$= 0 \qquad \text{if } S_{max}(\xi^{(n)}) \le Z^{(n)}. \quad (49)$$

The ensemble average $\langle Z \rangle_N$ is defined by

$$\langle Z \rangle_N \equiv \frac{1}{N} \sum_{n=1}^{N} Z^{(n)}, \quad (50)$$

and similarly for $\langle S \rangle_N$.

Recalling that stable combustion requires $\langle Z \rangle$ to balance $\langle S \rangle$ (Eq. 31), we suppose that global extinction occurs if

$$P_N(\xi^*, \mathrm{Da}) \equiv \mathrm{Prob}\{\langle Z \rangle_N > \langle S \rangle_N\}. \quad (51)$$

exceeds a critical value, P_{crit}. For Specified N and P_{crit}, this criterion defines the predicted stability boundary $\mathrm{Da}_{crit}(\xi^*)$ by the implicit relation

$$P_N(\xi^*, \mathrm{Da}_{crit}(\xi^*)) = P_{crit} \quad (52)$$

For $N = 50$ and $P_{crit} = 0.02$, the predicted stability boundary $\mathrm{Da}_{crit}(\xi^*)$ (determined by Monte Carlo) is shown on Fig. 14; and it may be seen that this crude model reproduces the DNS results.

It is emphasized that this model is presented merely to demonstrate that the observed discrepancies between DNS and standard models can plausibly be attributed to fluctuations in volume-averaged statistics. The model for reaction (Eq. 49) is at best a gross approximation; and obviously the model parameters (N and P_{crit}) were chosen to produce the desired result. Further research is needed to test the hypothesis offered here.

7. STATISTICAL DISTRIBUTIONS

In this section, results of simulations are presented to show the qualitatively different statistical distributions that exist at different Damkohler numbers. The specific results presented are scatter plots involving ξ, y, χ, Z, and S, all from simulations with $\xi^* = 0.517$. Except as noted below, each scatter plot consists of 4,096 samples, taken from a uniform 16^3 mesh of points in physical space.

First, we contrast results obtained from two simulations with Damkohler numbers of 93.2 and 18.6. With $\xi^* = 0.517$, the extinct range is deemed to be $(\mathrm{Da}_l, \mathrm{Da}_u) = (20, 60)$ (see Table 4). Hence Da = 93.2 is a relatively high Damkohler number, and the simulation yields statistically stationary fields corresponding to stable combustion. On the other hand, Da = 18.6 is below the extinction limit and, if the simulation were continued for long enough, there would certainly be global extinction. However, the fields are examined at $t/T_\chi = 6.5$, in the quasi-stationary state preceding extinction (see Fig. 12). Primary statistics characterizing the two simulations are given in Table 5.

For the high Damkohler number case (Da = 93.2), Fig. 17 shows scatter plots of $y/\langle y \rangle$, $Z/\langle Z \rangle$, $S/\langle Z \rangle$, and $(Z - S)/\langle Z \rangle$, all against ξ. It should be noted that for this case $\langle y \rangle$ is very small ($\langle y \rangle = 0.0036$), so that perturbation

TABLE 5

Summary of Primary Statistics from Simulations with $\xi^* = 0.517$ and Da = 18.6 and 93.2

N—grid size	N	64	64
ξ^*—$\xi'/\Delta\xi_r$	ξ^*	0.517	0.517
Da—Damkohler number	Da	18.6	93.2
T—duration of run	T/T_χ	16.4	26.3
$\langle Z \rangle$—mean mixing rate	$\langle Z \rangle T_\chi$	0.086	0.086
$\langle S \rangle$—mean reaction rate	$\langle S \rangle T_\chi$	0.075	0.086
$\langle y \rangle$—mean perturbation	$\langle y \rangle$	9.9×10^{-2}	3.6×10^{-3}
$\langle \chi \rangle$—mean scalar dissipation	$\langle \chi \rangle / \chi_F$	0.46	0.091
p_F—probability of local extinction (flamelet)	p_F	0.118	1.2×10^{-3}
p_Q—probability of local extinction (QEDR)	p_Q	0.116	1.5×10^{-3}

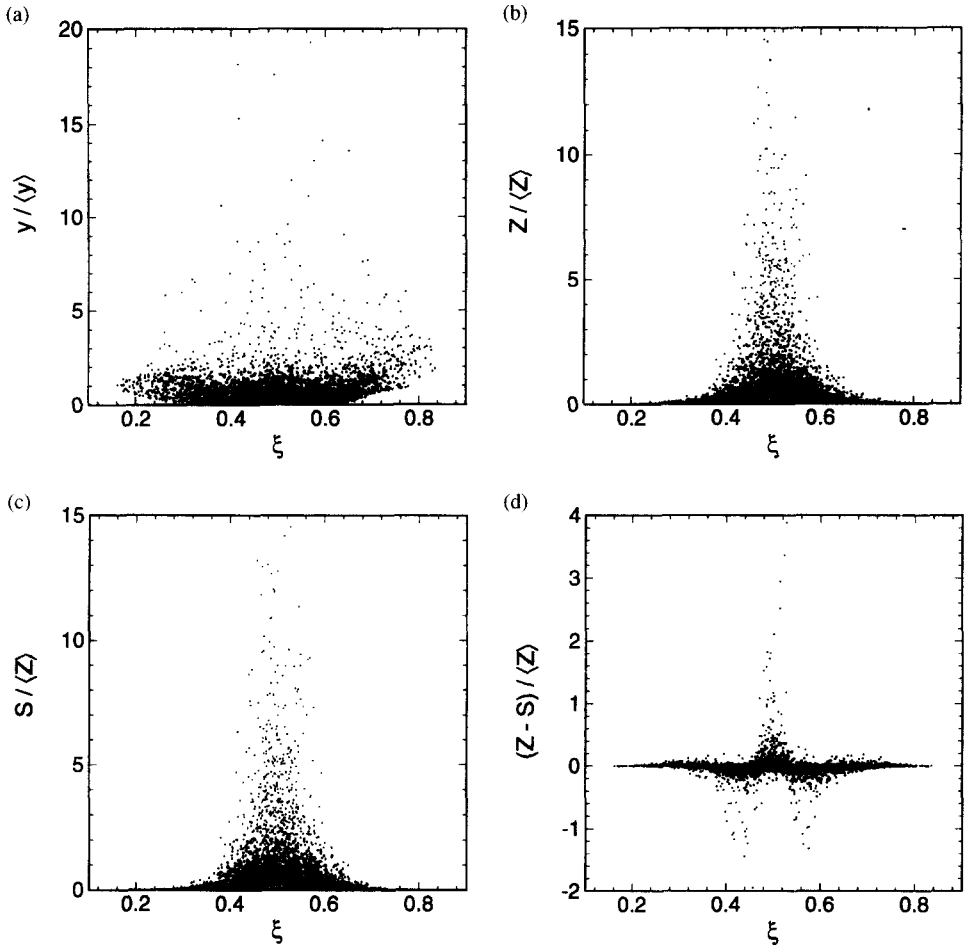

Fig. 17. Scatter plots of different statistics against mixture fraction from simulation with $\xi^* = 0.517$, Da = 93.2. (a) normalized perturbation $y/\langle y\rangle$. (b) normalized mixing rate $Z/\langle Z\rangle$. (c) normalized reaction rate $S/\langle Z\rangle$. (d) normalized imbalance between mixing and reaction $(Z - S)/\langle Z\rangle$.

of, say, $y = 10\langle y\rangle = 0.036$ are still quite small, signifying small departures from equilibrium. The normalized mixing rate $Z/\langle Z\rangle$ is negligible outside the reaction zone ($\xi_l = 0.38 < \xi < \xi_r = 0.62$) since $Y_e''(\xi)$ is negligible there. The scatter plot of $S/\langle Z\rangle$ appears very similar to that of $Z/\langle Z\rangle$, not by coincidence: the QEDR theory predicts $S = Z$. This prediction is tested directly by the scatter plot of $(Z - S)/\langle Z\rangle$. Indeed it may be observed that $(Z - S)$ is typically one order of magnitude less than Z, confirming the QEDR result.

Figure 18 examines the QEDR and flamelet predictions of the perturbation, y. Let ξ and χ be the mixture fraction and scalar dissipation at any point in the flow. Then if χ is less that the quenching value (i.e. $\chi < \chi_Q(\xi)$), QEDR predicts that y equals $y_Q(\xi, \chi)$, where the function $y_Q(\xi, \chi)$ is defined by Eq. 45. Figure 18a is the scatter plot of $(y - y_Q(\xi, \chi)/\langle y\rangle$ versus ξ, for the subset of points satisfying $\chi < \chi_Q(\xi)$. For this case, nearly all of the 4,096 points are included, since $p_Q \equiv \text{Prob}\{\chi > \chi_Q(\xi)\}$ is less than 1% (see Table 5). Similarly, Fig. 18b refers to the flamelet model prediction $y_F(\xi, \chi)$ for all samples satisfying $\chi < \chi_F$. It may be seen from Fig. 18 that the models are accurate for this case, with the departures $|y - y_F|/\langle y\rangle$ and $|y - y_Q|/\langle y\rangle$ seldom exceeding 0.2.

On closer examination of $(Z - S)/\langle Z\rangle$ (Fig. 17) and of $(y - y_Q)/\langle y\rangle$ (Fig. 18a), a pattern in the scatter is evident: the sample points are predominately positive around $\xi = \xi_s = 0.5$,

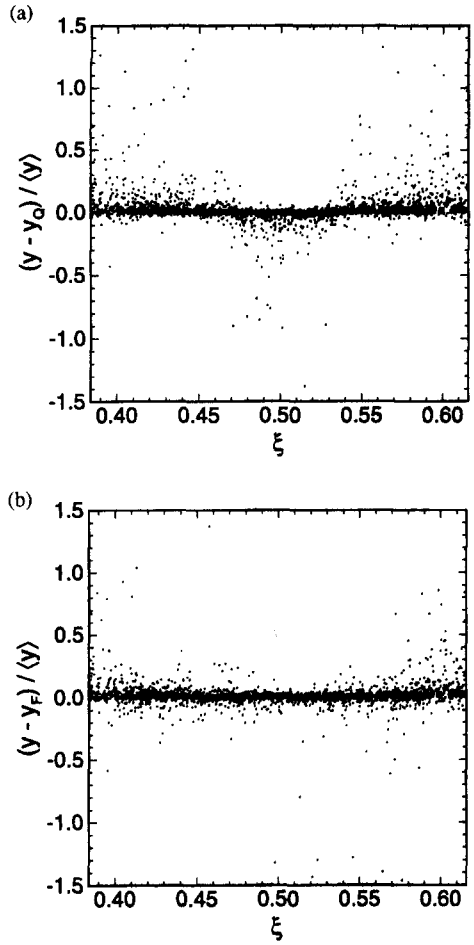

Fig. 18. Scatter plots of the perturbation y relative to QEDR and flamelet model predictions, against mixture fraction. From simulation with $\xi^* = 0.517$, Da = 93.2. (a) normalized departure from QEDR prediction $(y - y_Q(\xi, \chi))/\langle y \rangle$. (b) normalized departure from flamelet model prediction $(y - y_F \xi, \chi)/\langle y \rangle$.

while they tend to be negative around $\xi = \xi_l$ and $\xi = \xi_r$. This is likely because the diffusion term $\Gamma \nabla^2 y$ is not negligible in the balance of y (as supposed by the QEDR model), but rather it transports y away from where it is maximum (i.e., near $\xi = \xi_S$). The flamelet model accounts more completely for diffusion, and indeed the pattern mentioned above is not observable in the scatter plot of $(y - y_F)/\langle y \rangle$, Fig. 18b.

The same statistics are now examined for the low Damkohler number case (Da = 18.2), and a very different picture emerges. The mean of y is about 30 times larger ($\langle y \rangle \approx 0.1$) and the scatter plot of y (Fig. 19) shows values in excess of 0.4. Since Z is independent of Da, the scatter plot of $Z/\langle Z \rangle$ for this Damkohler number (Fig. 19b) is statistically identical to the higher-Damkohler number result (Fig. 17b): though rare, some samples of $Z/\langle Z \rangle$ exceed 10. The scatter plot of $S/\langle Z \rangle$ no longer appears the same as that of $Z/\langle Z \rangle$. Instead, the sample points are clearly confined in a compact region. The observed upper bound is simply the maximum possible reaction rate, $S_{\max}(\xi) = g(\xi)/\tau_c$. It is evident from the scatter plot of $(Z - S)/\langle Z \rangle$ that there are large departures from the QEDR balance $Z \approx S$.

From Fig. 20 it may be observed that there is some concentration of sample points about the model predictions (i.e., $y - y_Q = 0$ and $y - y_F = 0$), but there is also significant probability of large departures.

On Fig. 21 we compare the (S, ξ) scatter plots for the two cases, and show the conditional reaction rates. The quantity $[S(\xi, y)|\xi]$ is the volume-average reaction rate conditioned on ξ; while $[S(\xi, [y|\xi])|\xi]$ is the conditional average of S evaluated at the conditional mean y, $[y|\xi]$. According to the conditional moment closure, these quantities are equal because (it is assumed) the fluctuations in y about $[y|\xi]$ are small. For the high Damkohler number case, the two conditional means are indeed close to each other, but not for the reason supposed in CMC. For, an examination of Fig. 17 reveals significant fluctuations in y at any given ξ. Rather, the quantities are approximately equal because, over the small range of y encountered ($0 < y < 0.01$), the reaction rate $S(\xi, y)$ varies essentially linearly with y. For the lower Damkohler number case, on the other hand, the range of y is much larger, spanning the peak in $f(y)$ which occurs at $B^{-1} \approx 0.07$. Hence the two conditional means of S differ significantly, by more than a factor of 2.

To provide further insight into the qualitative changes with Da, a simulation (with $\xi^* = 0.517$) was performed in which the Damkohler number was quasi-statistically reduced from an initially high value (just as described in Section 5, Table 4). Scatter plots are now presented, taken from this simulation at times when the Damkohler number is 144, 55, 21.4, and 3.2.

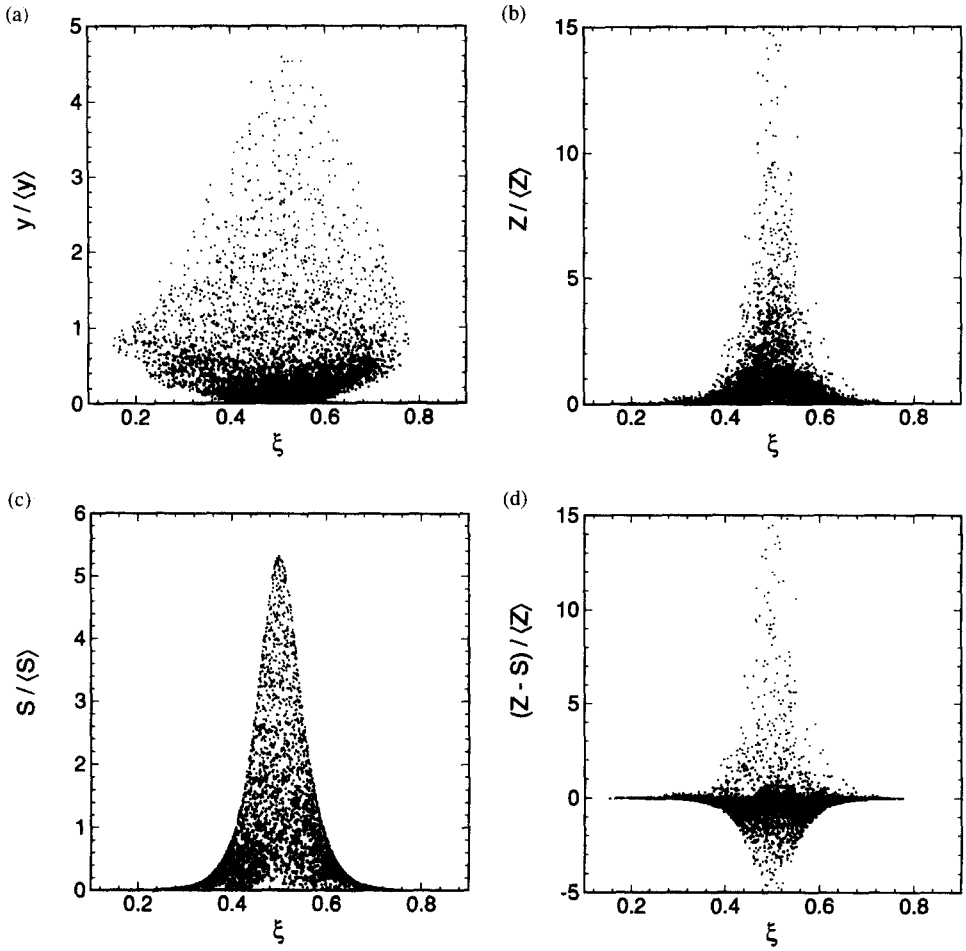

Fig. 19. Scatter plots of different statistics against mixture fraction from simulation with $\xi^* = 0.517$, Da = 18.2.

Figure 22 is a scatter plot of the normalized imbalance $(Z - S)/\langle Z\rangle$, and ξ. At the highest Damkohler numbers (Da = 144 and Da = 55), there is a small amount of scatter about zero, with the characteristic pattern mentioned above. At Da = 21.4, the scatter is greater—maybe by a factor of 3—and the distinctive pattern has disappeared. At stoichiometric, although the distribution is positively skewed, there are significant negative fluctuations. At the lowest Damkohler (Da = 3.2) reaction is almost negligible, and consequently the scatter plot resembles that of $Z/\langle Z\rangle$.

The scatter plot just described (Fig. 22) shows how the imbalance $Z - S$ varies with ξ. To investigate how the imbalance varies with the magnitude of Z itself, on Fig. 23 we show scatter plots of $S/\langle Z\rangle$ against $Z/\langle Z\rangle$. If there is perfect balance (as assumed in QEDR), then the sample point lies on the diagonal line indicated in the figure. At the highest Damkohler number (Da = 144), up to $Z/\langle Z\rangle = 15$ the small amount of scatter appears evenly distributed about the 45° line. But for the most intense mixing events ($Z/\langle Z\rangle > 15$), Z consistently exceeds S. At the next Damkohler number (Da = 55), the same pattern is evident, but now Z consistently exceeds S for $Z/\langle Z\rangle > 10$. By Da = 21.4 the pattern has changed. At this Damkohler number, the maximum possible reaction rate is $S/\langle Z\rangle \approx 6$. Hence, as is evident from the figure, for $Z/\langle Z\rangle$ greater than 6, it is impossible for the sample points to lie on the 45° line. There is also a difference at the lowest mixing values: evidently there are many sample points signifi-

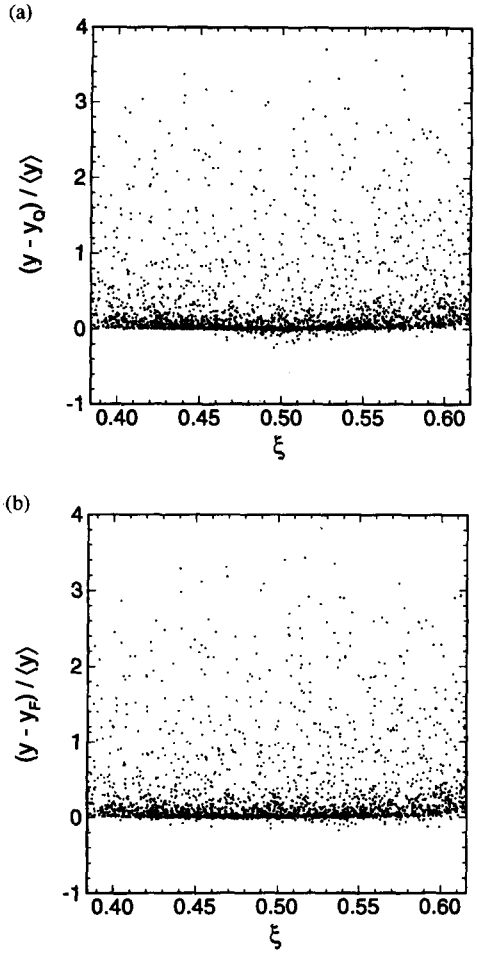

Fig. 20. Scatter plots of the perturbation y relative to QEDR and flamelet model predictions, against mixture fraction. From simulation with $\xi^* = 0.517$, Da = 18.2.

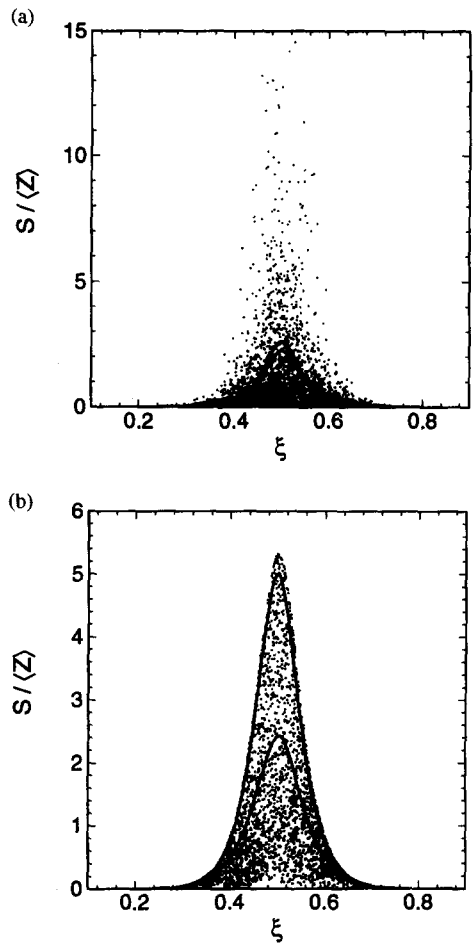

Fig. 21. Scatter plots of normalized reaction rate $S/\langle Z\rangle$ against ξ from simulations with $\xi^* = 0.517$ and (a) Da = 93.2, (b) Da = 18.2. Lower line, conditional mean reaction rate $[S(\xi, y)|\xi]$; upper line, reaction rate based on conditional mean $[S(\xi,[y|\xi])|\xi]$.

cantly above the 45° line. Thus, as Da is decreased, the local balance between mixing and reaction breaks down first for high values of Z, but close to the extinction limit the breakdown occurs for small Z also. At the lowest value of Da, reaction is negligible, resulting in the sample points lying close to the $Z/\langle Z\rangle$ axis.

Figures 24 and 25 show the perturbation y, and the discrepancy in the flamelet model prediction $y - y_F$ for the four Damkohler numbers. It should be recalled that in the $y - y_F$ vs. ξ scatter plot (Fig. 25) only those samples with $\chi < \chi_F$ are shown. Hence although it is not surprising to see the discrepancy increase with decreasing Damkohler number, for the samples shown, locally a flamelet structure is possible.

8. QUANTITATIVE ASSESSMENT OF MODELS

We now quantify the accuracy of the flamelet and QEDR models over the range of ξ^* and Da investigated.

Both models predict local extinction if the scalar dissipation exceeds a particular quenching value. The probability of local extinction for the flamelet model is defined, then, by

$$p_F \equiv \text{Prob}\{\chi > \chi_F | \xi_l < \xi < \xi_r\}. \tag{53}$$

And for the QEDR model it is

$$p_Q \equiv \text{Prob}\{\chi > \chi_Q(\xi) | \xi_l < \xi < \xi_r\}. \tag{54}$$

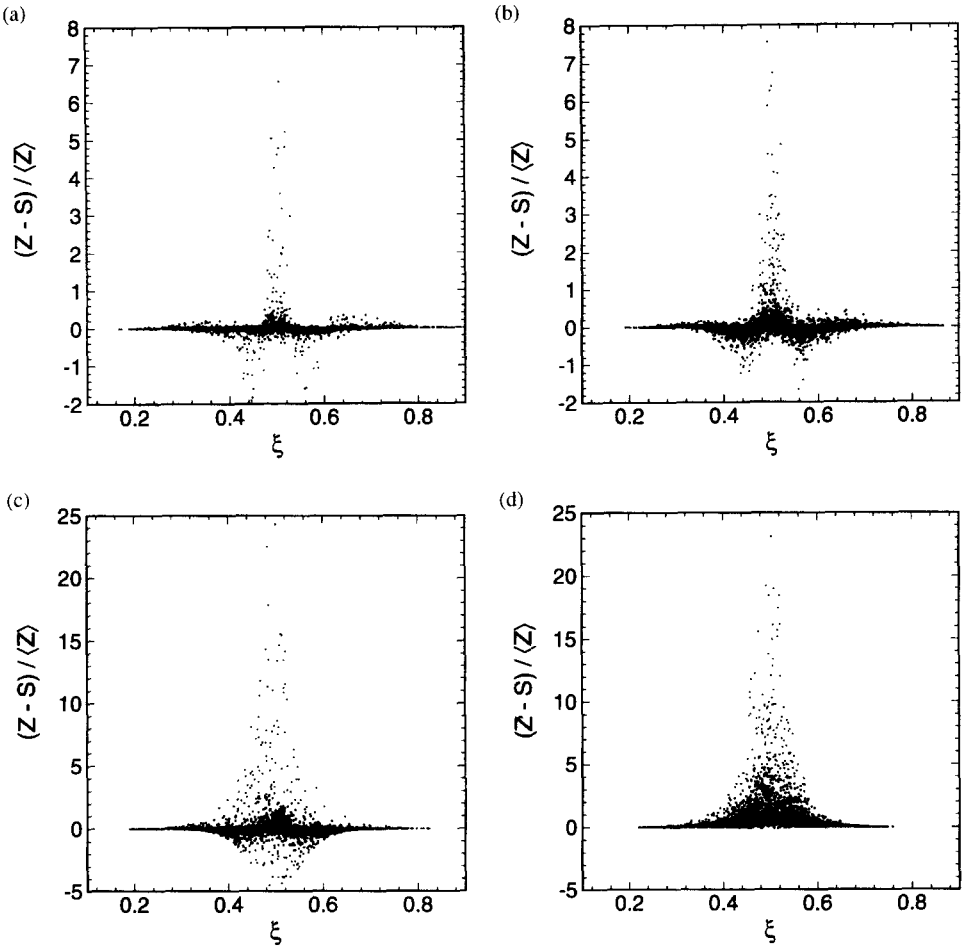

Fig. 22. Scatter plots of the normalized imbalance between mixing and reaction $(Z - S)/\langle Z\rangle$ against mixture fraction, ξ, for a simulation with $\xi^* = 0.517$ and Da decreasing quasi-statistically. (a) Da = 144, (b) Da = 55, (c) Da = 21.4, (d) Da = 3.2.

Next we define the regions in $\xi - \chi$ space where the models can be expected to be valid. For the flamelet model the region of validity is

$$\mathscr{R}_F \equiv \{(\xi, \chi): \chi < \chi_F, \xi_l < \xi < \xi_r\}, \tag{55}$$

and similarly for QEDR

$$\mathscr{R}_Q \equiv \{(\xi, \chi): \chi < \chi_Q(\xi), \xi_l < \xi < \xi_r\}. \tag{56}$$

Two error indices are used to quantify the discrepancy between flamelet model predictions and the DNS result: the *fractional error in the conditional mean*

$$\delta_F \equiv [(y_F - y)|\mathscr{R}_F]/[y|\mathscr{R}_F], \tag{57}$$

and the *rms normalized error*,

$$\epsilon_F \equiv \left[(y_F - y)^2/\max(y_F, y)^2|\mathscr{R}_F\right]^{1/2}. \tag{58}$$

For QEDR, δ_Q and ϵ_Q are defined in the same way.

It is important to recognize that the probability of local extinction and the error indices are quantifying different aspects of performance. For reactive fluid ($\xi_l < \xi < \xi_r$), p_F measures the probability that the flamelet model is inapplicable (i.e., $\chi > \chi_F$); whereas the error indices measure the accuracy of the model *where it is applicable* (i.e., $\chi < \chi_F$).

Figure 26 shows the quantities defined above for the simulation with $\xi^* = 0.517$ and with the Damkohler number decreasing quasi-stat-

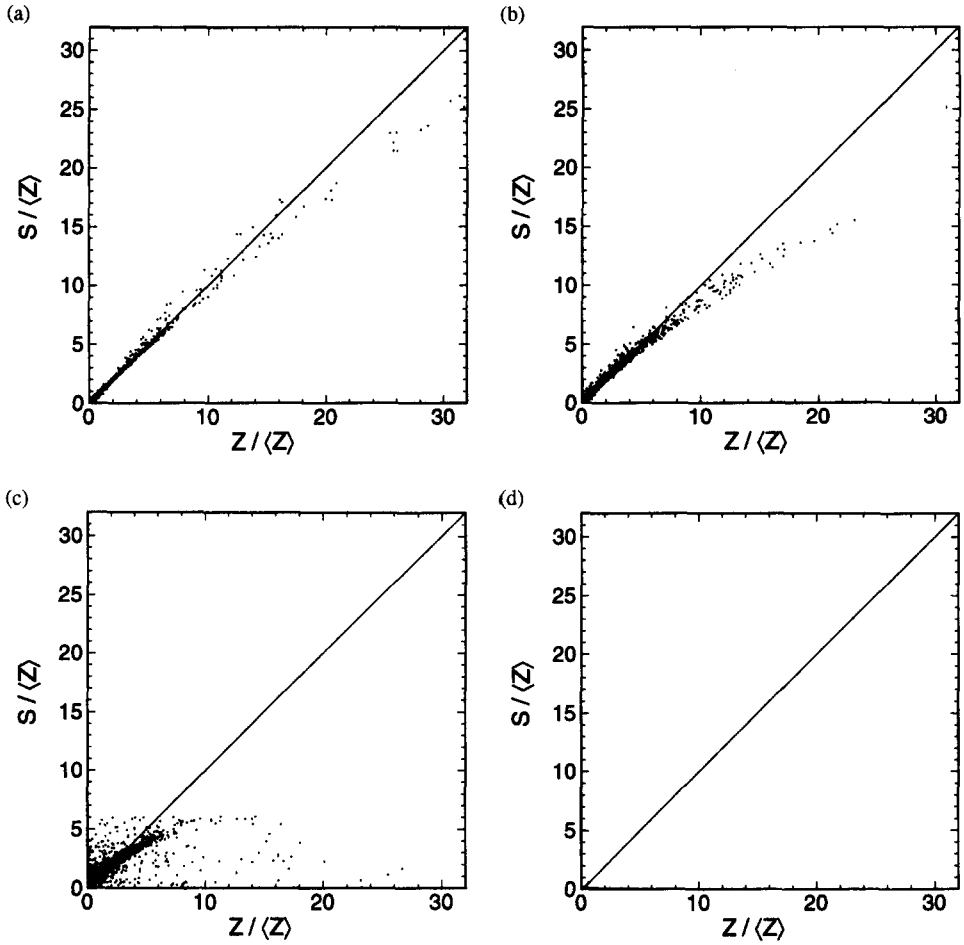

Fig. 23. Scatter plots of normalized reaction rate $S/\langle Z\rangle$ against normalized mixing rate $Z/\langle Z\rangle$ for fraction, ξ, for a simulation with $\xi^* = 0.517$ and Da decreasing quasi-statistically. (a) Da = 144, (b) Da = 55, (c) Da = 21.4, (d) Da = 3.2. The solid diagonal line corresponds to a balance between reaction and mixing, i.e., $S = Z$.

istically from an initially-large value. It may be seen that there is little difference between the performance of the two models: hence we describe the performance of the flamelet model, but the observations apply equally to QEDR.

At the highest Damkohler number p_F and δ_F are essentially zero, while ϵ_F shows an rms error slightly over 10%. At the lowest Damkohler number there is local extinction almost everywhere ($p_F \approx 1$), and, with y increasing without bound, δ_F and ϵ_F asymptote to -1 and 1, respectively.

Most flamelet models that attempt to incorporate effects of extinction (e.g. Peters 1984) assume that the occurrence of local extinction for some flamelets (with $\chi > \chi_F$) does not affect the properties of the remaining flamelets ($\chi < \chi_F$). But the results shown on Fig. 26 clearly refute this assumption. For, as Da decreases the error indices rise and become appreciable while p_F increases more slowly. This observation is reinforced by Fig. 27 which shows ϵ_F plotted against p_F for simulations with different values of ξ^*, and with Da decreasing quasi-statistically. It may be seen that, in all cases, the r.m.s. error ϵ_F exceeds 40% before the probability of local extinction p_F exceeds 10%.

These simulations are used to identify the region of validity of the flamelet and QEDR models on the Da $-$ ξ^* plane. We define $\mathrm{Da}_{0.1}(\xi^*)$ and $\mathrm{Da}_{0.5}(\xi^*)$ as the values ofm-

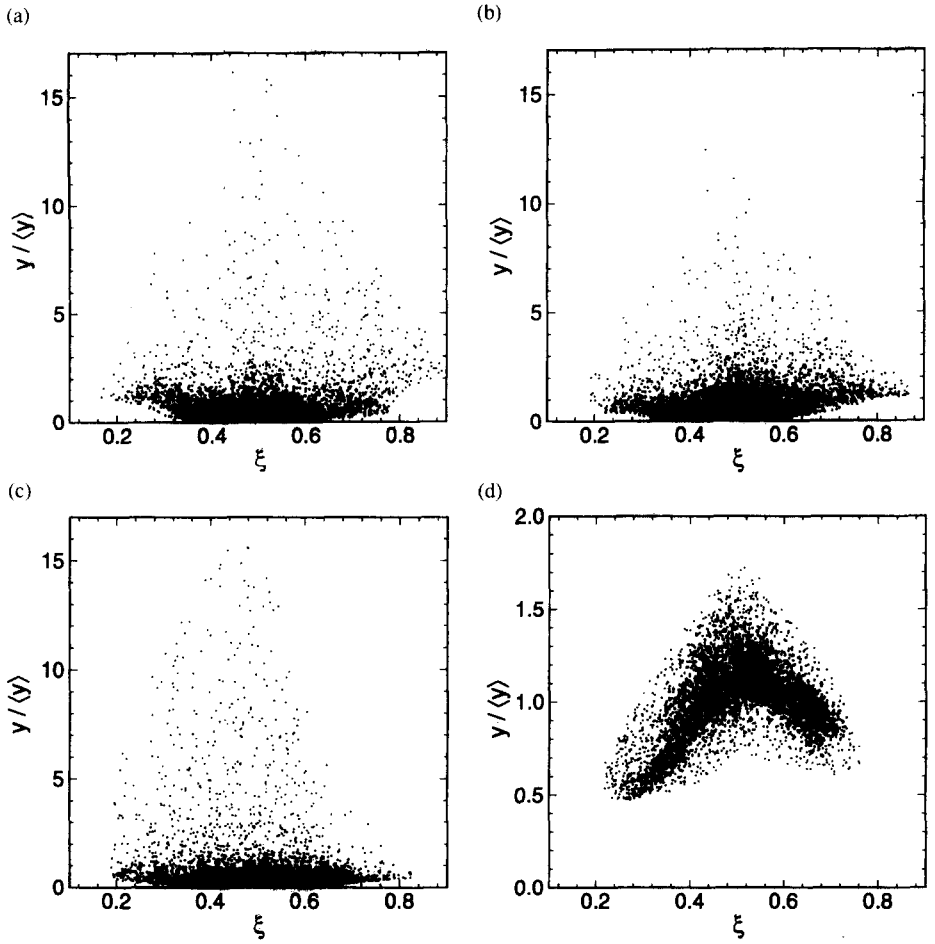

Fig. 24. Scatter plot of $y/\langle y\rangle$ against mixture fraction, ξ, for a simulation with $\xi^* = 0.517$ and Da decreasing quasi-statistically. (a) Da = 144, (b) Da = 55, (c) Da = 21.4, (d) Da = 3.2.

Damkohler number at which the error in the predicted conditional mean δ_F equals 0.1 and 0.5, respectively. Their values are plotted in Fig. 14. It may be seen that there is a close correspondence between the range ($Da_{0.1}$, $Da_{0.5}$) and the extinction range (Da_l, Da_u).

It can be argued that the flamelet model is inapplicable for small ξ^* (i.e. broad reaction zones, e.g. Bilger [6]); and certainly its accuracy is expected to increase as ξ^* increases. This is indeed observed in Fig. 27. For very small p_F —and hence large Da—the rms error, ϵ_F, is about 40% for $\xi^* = 0.172$, but is just 10% for $\xi^* = 1.552$.

9. SUMMARY AND CONCLUSIONS

Direct numerical simulations have been performed in order to study fundamental processes in non-premixed turbulent reacting flows. A simple thermochemical model for one-step reversible reactions is employed, in which the state of the fluid is described by the mixture fraction $\xi(\mathbf{x}, t)$ and the perturbation from equilibrium $y(\mathbf{x}, t)$. A pseudo-spectral method, with grid sizes up to 128^3, is used to solve the Navier-Stokes equations and the conservation equations for ξ and y. These equations are augmented by artificial forcing, so that the resulting velocity and mixture fractions fields are statistically stationary, homogeneous, and isotropic. At sufficiently high Damkohler number, Da, the perturbation field, y, is also statistically stationary—corresponding to stable combustion. But at low Damkohler number, y increases without bound—corresponding to global extinction.

The three most important non-dimensional

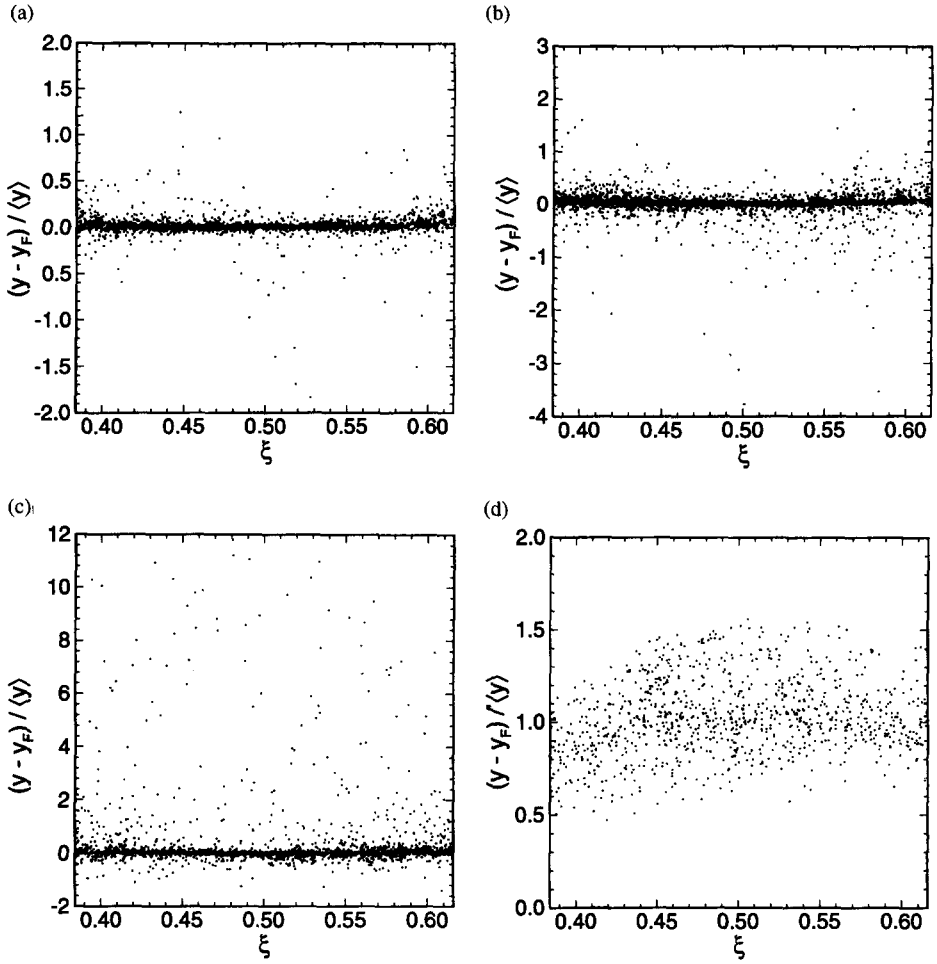

Fig. 25. Scatter plot of the discrepancy in the flamelet model prediction $(y - y_F(\xi, \chi))/\langle y \rangle$ against mixture fraction ξ. From simulation with $\xi^* = 0.517$, and Da decreasing quasi-statistically. (a) Da = 144, (b) Da = 55, (c) Da = 21.4, (d) Da = 3.2.

parameters characterizing the simulations are: the Taylor-scale Reynolds number, R_λ; the Damkohler number Da; and, ξ^* defined as the ratio of the r.m.s. mixture fraction, ξ', to the reaction-zone thickness in mixture-fraction space $\Delta\xi_r$. The range of ξ^* studied—$\xi^* = 0.172$ to $\xi^* = 1.552$—goes from broad, to relatively narrow reaction zones in physical space. For the narrowest reaction zones ($\xi^* = 1.552$), the numerical resolution requirements for the y field are approximately 8 times those of the velocity and ξ fields. In consequence, with a practical computational limit on grid size of 128^3, the rather low Reynolds number $R_\lambda = 17$ is selected so that indeed the y field is well resolved. There is no difficulty in studying all values of Da of interest.

In an overly simple view, global extinction is characterized by the function $\mathrm{Da}_{\mathrm{crit}}(\xi^*)$: for $\mathrm{Da} > \mathrm{Da}_{\mathrm{crit}}$ there is stable combustion; for $\mathrm{Da} < \mathrm{Da}_{\mathrm{crit}}$ there is global extinction. The standard models (flamelet, QEDR and CMC) make similar predictions of $\mathrm{Da}_{\mathrm{crit}}(\xi^*)$; in particular that $\mathrm{Da}_{\mathrm{crit}}$ scales as ξ^{*2}. The simulation results (e.g., Fig. 12) demonstrate that the phenomenon is more complex, because of statistical variability. Consequently, in place of $\mathrm{Da}_{\mathrm{crit}}(\xi^*)$, we estimate an extinction range, with lower and upper Damkohler number values, $\mathrm{Da}_l(\xi^*)$ and $\mathrm{Da}_u(\xi^*)$. In spite of the imprecision in Da_l, it is found that qualitatively and quantitatively the DNS results differ from the model predictions: Da_l scales as $\xi^{*2.3}$, and exceeds $\mathrm{Da}_{\mathrm{crit}}$ (given by the models) by up

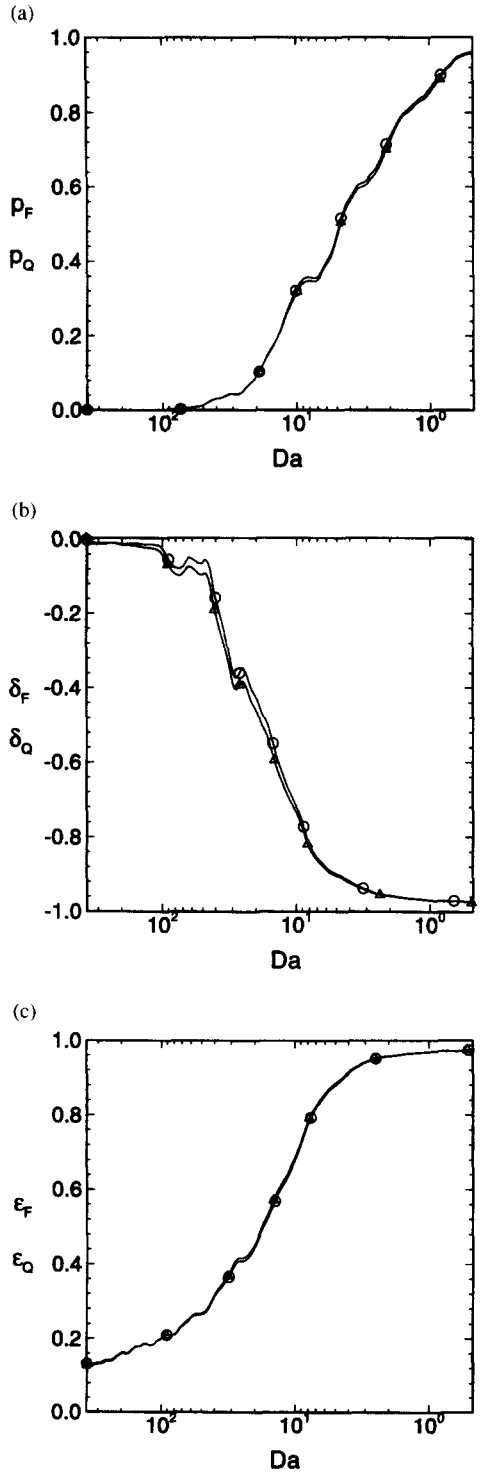

Fig. 26. Model performance indices against Da, for simulation with $\xi^* = 0.517$ and Da decreasing quasi-statistically. (a) Probability of local extinction: flamelet model p_F, ○; QEDR p_Q, △. (b) Fractional error in conditional mean, δ_F, ○; δ_Q, △. (c) rms normalized error: ϵ_F, ○; ϵ_Q, △.

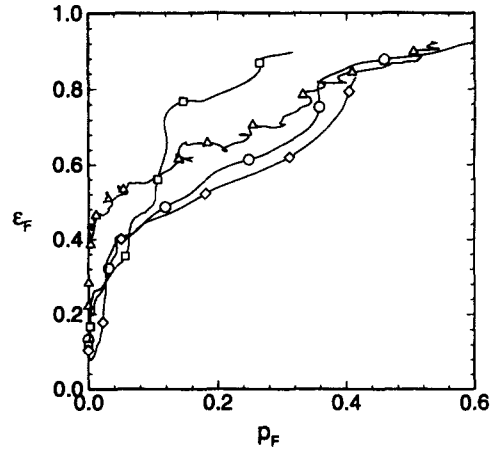

Fig. 27. The r.m.s. normalized error, ϵ_F, against probability of local extinction, p_F, from simulations with Da decreasing quasi-statistically: $\xi^* = 0.172$, △; $\xi^* = 0.517$, ○; $\xi^* = 1.0$, □; $\xi^* = 1.552$, ◇.

to a factor of 4 (see Fig. 14). A simple statistical model is used to show that the discrepancies can plausibly be explained by statistical variability.

At large Damkohler number ($\mathrm{Da} \gg \mathrm{Da}_u(\xi^*)$) it is found that both flamelet and QEDR models accurately describe the perturbation field $y(\mathbf{x}, t)$ in terms of the mixture fraction field $\xi(\mathbf{x}, t)$. But as Da is decreased towards Da_u significant discrepancies emerge. It is expected that a simple flamelet structure does not exist where the scalar dissipation χ exceed the flamelet quenching value χ_F. The probability of this occurrence, p_F, increase as Da decreases. But perhaps unexpectedly, it is found that the flamelet model prediction at locations with $\chi < \chi_F$ deteriorates very significantly even when p_F is not large. For example with $p_F = 0.1$ the model error exceeds 40%. The Damkohler numbers $\mathrm{Da}_{0.1}$ and $\mathrm{Da}_{0.5}$ at which the model errors are 10% and 50% correlate well with Da_u and Da_l (see Fig. 14).

This work was supported by Grant DE-FG02-90ER14128 from the U.S. Department of Energy, Chemical Sciences Division.

REFERENCES

1. Bilger, R. W., in *Turbulent Reacting Flows: Topics in Applied Physics*, (P. A. Libby and F. A. Williams, Eds.), Springer, Berlin, 1980, pp. 65–113.

2. Bilger, R. W., *Annu. Rev. Fluid Mech.* 21:101–135 (1989).
3. Peters, N., *Prog. Energ. Combust. Sci.* 10:319–339 (1984).
4. Correa, S. M., Drake, M. C., Pitz, R. W., and Shyy, W., *Twentieth Symposium (International) on Combustion*, The Combustion Institute, Pittsburgh, 1984, pp. 337–343.
5. Pope, S. B., and Correa, S. M., *Twenty-first Symposium (International) on Combustion*, The Combustion Institute, Pittsburgh, 1986, p. 1341.
6. Bilger, R. W., *Twenty-Second Symposium (International) on Combustion*, The Combustion Institute, Pittsburgh 1988, pp. 475–488.
7. Bilger, R. W., Conditional moment methods for turbulent reacting flows using Crocco variable conditions. Charles Kolling Research Laboratory TN F-99, The University of Sydney, February 1991.
8. Klimenko, Y., *J. Fluid Dyn.* 25:327–334 (1990).
9. Masri, A. R., Dibble, R. W., and Barlow, R. S., *Combust. Flame* 91:285–309 (1992).
10. Chen, J.-Y., and Kollmann, W., *Twenty-Second Symposium (International) on Combustion*, The Combustion Institute, Pittsburgh, 1988, pp. 546–653.
11. Taing, S., Masri, A. R., and Pope, S. B., *Combust. Flame* 95:133–150 (1993).
12. Norris, A. T., and Pope, S. B., *Combust. Flame* 100:211–220 (1995).
13. Yeung, P. K., and Pope, S. B., *J. Fluid Mech.* 207:531–586 (1989).
14. Esaran, V. and Pope, S. B., *Comput. Fluids* 16:257–278 (1988).
15. Eswaran, V. and Pope, S. B., *Phys. Fluids* 31:506–520 (1988).
16. Rogallo, R. S., NASA TM 81315 (1981).
17. Gibson, H. C., *Phys. Fluids* 11:2316 (1968).
18. Tennekes, H., and Lumley, J. L., *A First Course in Turbulence*, M.I.T. Press, Cambridge, MA (1972).
19. Pope, S. B., *Annu. Rev. Fluid Mech.* 19:237–270 (1987).
20. Pope, S. B., *Twenty-Third Symposium (International) on Combustion*, The Combustion Institute, 1990, pp. 591–612.
21. Lee, Y.-Y., Ph.D. thesis, Cornell University, 1994.
22. Giovangigli, V., Smooke, M. D., Report ME-102-89, Yale University (1989).
23. Chan, T. F., *SIAM J. Sci. Stat. Comput.* 5:135–148 (1984).
24. Peters, N., and Williams, F. A., *AIAA J.* 21:423–429 (1983).
25. Bilger, R. W., in *Turbulence and Molecular Processes in Combustion* (T. Takeno, Ed.) Elsevier, Amsterdam, 1993, pp. 267–285.
26. Mell, W. E., Nilsen, V., Kosály, G., and Riley, J. J., *Phys. Fluids* 6:1331–1356, (1994).

Received 1 March 1994; revised 17 October 1994.